First Principle Study of Structural, Electronic and Magnetic Properties of Doped $TbMnO_3$ for Transportation in Spintronic Devices

By

Sayyda Rimsha Irfan

CIIT/SP22-RPH-023/LHR

MS Thesis

In

MS Physics

COMSATS University Islamabad,
Lahore Campus- Pakistan

FALL, 2023

COMSATS University Islamabad

First Principle Study of Structural, Electronic and Magnetic Properties of Doped $TbMnO_3$ for Transportation in Spintronic Devices

A Thesis Presented to

COMSATS University Islamabad, Lahore Campus

In partial fulfillment

of the requirement for the degree of

MS (Physics)

By

Sayyda Rimsha Irfan

CIIT/SP22-RPH-023/LHR

Fall, 2023

First Principle Study of Structural, Electronic and Magnetic Properties of Doped $TbMnO_3$ for Transportation in Spintronic Devices

---

A Post Graduate Thesis submitted to the Department of Physics as partial fulfillment of the requirement for the award of Degree of MS (Physics)

Name	Registration Number
Sayyda Rimsha Irfan	CIIT/SP22-RPH-023/LHR

Dr. Kashif Tufail

Associate Professor, Department of Physics

Lahore Campus

COMSATS University Islamabad

January, 2023

Final Approval

This thesis titled

First Principle Study of Structural, Electronic and Magnetic Properties of Doped $TbMnO_3$ for Transportation in Spintronic Devices

By

Sayyda Rimsha Irfan
CIIT/SP22-RPH-023/LHR
Has been approved

For the COMSATS University Islamabad, Lahore Campus

External Examiner: ____
Dr. Faheem Khurshied Butt
Associate Professor, Division of Science and Technology,
University of Education, Lahore

Supervisor: ____
Dr. Kashif Tufail
Associate Professor, Department of Physics, CUI, Lahore

Co-Supervisor: ____
Dr. Muhammad Imran
Associate Professor, Department of Physics, CUI, Lahore

HoD: ____
Prof. Dr. Hafiz Muhammad Ashfaq Ahmad
Head of Physics Department, CUI, Lahore Campus

Declaration

I, Sayyda Rimsha Irfan, **CIIT/SP22-RPH-023/LHR** hereby declare that I have produced this work, which is presented in this thesis, during the scheduled period of study. I also declare that I have not taken any material from any source except referred to wherever due. If a violation of HEC rules on research project has occurred in this thesis, I shall be liable to punishable action under the plagiarism rules of the HEC.

Date: ________________

Signature of the student:

____

Sayyda Rimsha Irfan
CIIT/SP22-RPH-023/LHR

Certificate

It is certified that Sayyda Rimsha Irfan, CIIT/SP22-RPH-023/LHR has carried out all the research work related to this thesis under my supervision at the Department of Physics, COMSATS University Islamabad, Lahore Campus and the work fulfills the requirement for award of MS degree.

Date: ________________

Supervisor:

____

Dr. Kashif Tufail
Associate Professor
Department of Physics
CUI, Lahore.

Head of Department:

____

Dr. Hafiz Muhammad Ashfaq Ahmad
Professor
Department of Physics
CUI, Lahore.

ACKNOWLEDGEMENT

In the name of Allah S.W.T, the Most Gracious and the Most Merciful,

All praises to Allah, for His Mercy have given me patience and strength to complete this research project.

I would like to express my deepest appreciation to my main supervisor, Dr. Kashif Tufail for his guidance and support in my research. This thesis would not be a success without his helpful suggestions and constructive comments from the start until final of this research. A special thanks also goes to Dr. Muhammad Tariq and co-supervisors Dr. Muhammad Imran for their continuous assistance.

I would like to extend my sincere gratitude to all lecturers and staff in the Department of Physics and fellow friends that had directly and indirectly helped me throughout my research project. I wish to mention each and every one of them, but the list is too long and the space is limited. I am also thankful to COMSATS University for giving me the opportunity to complete my research project. Last but not least, I am forever indebted and grateful to my precious parents, family and my loved ones for their endless motivation, understanding and encouragement. It is such a heart-warming experience I had, and such experience will always be with me. Thank you so much.

Sayyda Rimsha Irfan
CIIT/SP22-RPH-023/LHR

ABSTRACT

Multiferroic Terbium Magnate, $TbMnO_3$ (TMO), is one of the most investigated compounds for advances in spintronic devices. Single-phase multiferroic TMO can play an important role in the development of spintronics random access memory (RAM) due to its spin-polarized electronic, magnetic, and dielectric properties. However, the major challenge in the field of spintronic RAM technology is to generate a balanced magnetization of 25 MA/cm, more than 80% spin polarization at the Fermi level, and suitable dielectric constant in the range of 10 to 52. The present research work explores the structural, spin-polarized electronic, dielectric, and magnetic properties of Dysprosium (Dy) doped TMO structure for spintronic memory device application using first-principles calculations. The generalized gradient approximation (GGA) with Perdew-Burke-Ernzerhof (PBE) is used to perform numerical simulation using CASTEP numerical coding. Dy impurities in TMO structure change the lattice constant, volume, and bond length, which profoundly affects the material's properties. The band gap in the spin-up and spin-down states is altered by the inclusion of Dy atoms due to increase in the energy states. The additional energy levels significantly enhance the spin polarization at the Fermi level, which is more favorable for spintronic devices. The addition of Dy-dopants as mono, di and triatomic in Pure TMO 2x2x2 super cell results in decrease in the magnetic moment. The half metallicity or 86.3 % spin polarization at the Fermi level, high dielectric constant of 1520.65, appropriate magnetism of 34.69 MA/cm has been observed for triatomic Dy-doped TMO material in orthorhombic phase. Thus, triatomic Dy-doped TMO is a potential single-phase material spintronic ferro memory device applications.

TABLE OF CONTENTS

LIST OF FIGURES

LIST OF TABLES

LIST OF ABBREVIATIONS

AF	Antiferromagnetic
CV	Conduction band
CASTEP	Cambridge Serial Total Energy Package
DFT	Density functional theory
DOS	Density of states
E_F	Fermi Energy Level
GGA	Generalized gradient approximation
IBLC	Internal barrier layer capacitor
LDA	Local density approximation
LBFGS	Limited memory Broyden–Fletcher–Goldfarb–Shanno
MCE	Magnetocaloric effect
NCP	Norm conserving pseudopotential
OTFG	On the fly generated
PDOS	Partial density of states
RAM	Random access memory
RCFM	Reverse charge current from magnet
SOC	Spin-orbit coupling
SCF	Self-consistent field
TMO	Terbium Manganate
T_N	Neel Temperature
T_C	Curie Temperature
USP	Ultrasoft pseudopotential
VB	Valence band

LIST OF SYMBOLS

M_s	Total spin magnetic moment
$\varepsilon(0)$	Dielectric constant
M	Volume magnetization
P_s	Spin polarization
$g_n(E_F)_\uparrow$	DOS in spin-up
$g_n(E_F)_\downarrow$	DOS in spin down
Ω_o	per unit volume
$K(\omega)$	Excitation coefficient
$R(\omega)$	Reflectivity ,
$n(\omega)$	Refractive-index
$L(\omega)$	Loss function
$\alpha(\omega)$	Absorption-coefficient

CHAPTER 1

INTRODUCTION

1.1. Background:

One of the emerging fields to increase processing capabilities and memory while reducing their power consumption for the next generation nanoelectronics systems is Spintronics. Electrons/holes' spin degree of freedom which may also interact with their orbital moments is used in these devices. The spin polarization in these devices is controlled either via spin-orbit coupling or magnetic layers acting as spin analyzers or polarizers [1]. The Figure 1.1 shows connected vision of spintronics, electronics and ultimate memory device. Magnetic random access memory Computing devices based on spintronics technology would never loss their data, even if the powder suddenly went off. From this perspective, new possibilities toward the fabrication of the ultimate memory device are presented by the multiferroic materials, particularly magnetoelectric (ferroelectric-ferromagnetism coupling) material. [2]. Multiferroic materials are promising materials for memory devices because of their ability to convert spin current to charge current while preserving the data stored in spin polarization. The study of these materials has received a great attention in the last few years for their potential use in spintronics [3–6]. The multiferroic materials which are suitable for the spintronics application are $BiFeO_3$ [2, 3], $YMnO_3$ [4, 5] and $TbMnO_3$ [6, 7]. The magnetoelectric (ME) effect is a unique property of multiferroics that possess both ferroelectric and ferromagnetic simultaneously. The coupling between the two ferroic orders i.e. ferroelectricity and ferromagnetism is the cause of ME effect which enables one to modify its magnetic properties by an electric field and tune its electric properties by applying an external magnetic field. Multiferroics may find potential application in spintronics so study on these material is important [8, 9]. Introducing effective spin from a ferromagnet into a non-magnetic material is one of the main problems in spintronic materials. The passing electrons from ferromagnet into non-magnetic material degrade the spin polarization of ferromagnet dramatically. High temperature can change the spins of electrons by disturbing the magnetization of materials which creates errors. Additional there is no thermal stability spintronic materials. Temperature, magnetic symmetry, and crystal structure can significantly affect the threshold magnetism of material. Researchers are trying to find new material for an effective performance in spintronics with high threshold magnetism.

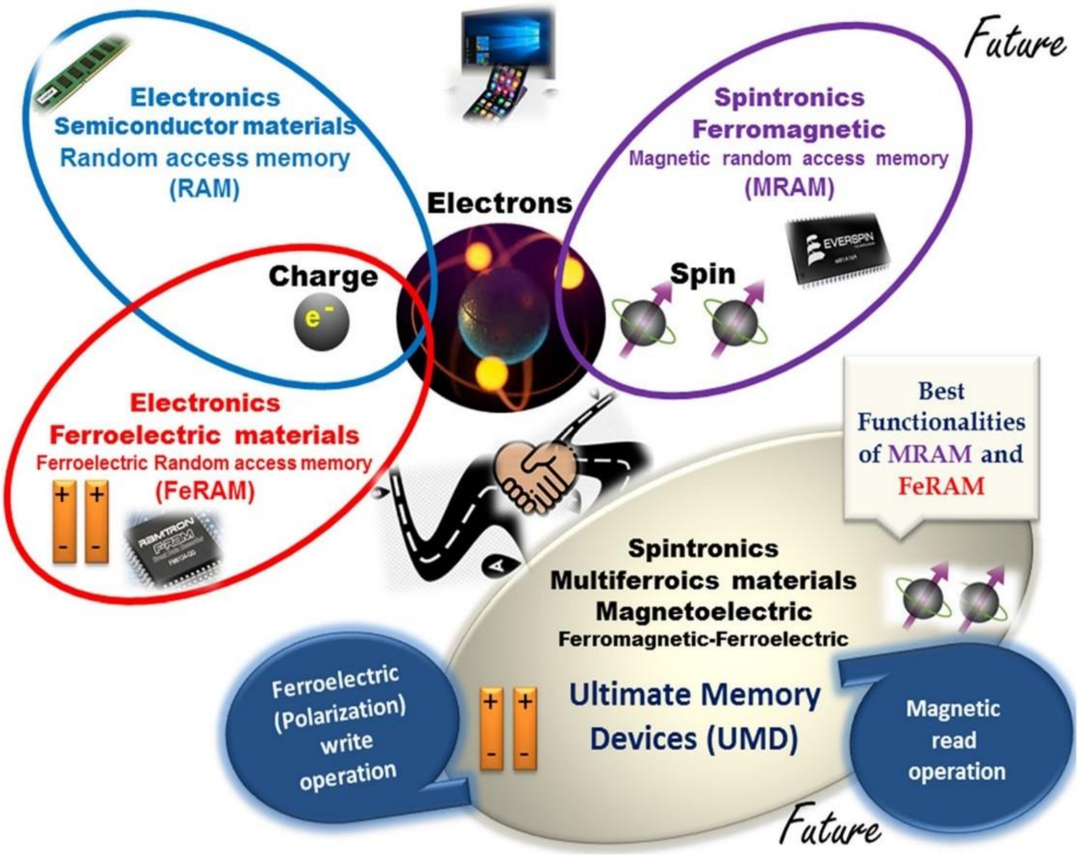

Figure 1.1: Connected vision of electronics, spintronics and ultimate memory device [2]

Researchers are increasingly interested in studying $RMnO_3$ (rare-earth manganite) due to its disordered orthorhombic crystal structure and strong magnetoelectric coupling. The properties of $TbMnO_3$ is expected to be enhanced by partly substituting Fe, Ca, Ti, Ga, Na, and La ions at Tb or Mn site. Due to extrinsic effects like internal barrier layer capacitor (IBLC), spatial inhomogeneity and contact effect originate the high dielectric constant by the dopants [10] which increased the focused on the doped TMO [9]. The substituting and doping in the multiferroic compound with various types of magnetic ions are often helpful experimental methods to enhance and control the different characteristics of the compound [11, 12].

Manganite materials have been the subject of research due to their affordability, stability and having low cost since the past decade. These materials also exhibit variety of properties such as spin lattice coupling, magnetoresistance, etc in addition to magnetocaloric effect (MCE). Recently $RMnO_3$ (R = Dy, Gd, Ho and Tb) materials have been reported to exhibit enhanced MCE through the magneto-electric coupling [13].

1.2 Problem Statement:

The magnetic transition of $TbMnO_3$ has Neel temperature of ~41 K and produce ferroelectric polarization of ~600 µC/m^2 at ~27 K. $TbMnO_3$ material is potential material for the spintronic applications due to its multiferroic nature. The drawback of $TbMnO_3$ material is high dielectric loss which make this material not fit for practical application [14]. The $TbMnO_3$ magnetic structure shows complex features. Early Tb^{3+} and Mn^{3+} investigations have found main three magnetic transitions which are caused by the magnetic moment ordering of the Mn^{3+} at low temperatures. At room temperature $TbMnO_3$ multiferroic shows paramagnetic behavior. The problem with $TbMnO_3$ multiferroic in technological applications is their extremely small value of ~100 µC/m^2 electric polarization and low Neel temperature ~27 K. $TbMnO_3$ is a typical multiferroic perovskite among all the known materials which exhibit clear relaxations at both high and low temperature with various processes [9, 10]. It is possible to improve the typically simple characteristics of conventional perovskite composite oxides by partially substituting ions at the Mn or Tb site [9].

Therefore, this work focuses on exploring the electronic, structural, magnetic and optical properties of pure and Dy doped $TbMnO_3$ for the applications of spintronic devices.

1.3 Objectives

The main goal of this project is to study the optical and magnetic properties of Terbium manganite by introducing Dy dopant at A-site ($Tb_{1-x}Dy_xMnO_3$) using Cambridge Serial Total Energy Package (CASTEP) for spintronics applications. Following are the specific objectives:

1) To optimize and calculate the structural properties (lattice parameters, bond angle and bond length) of pure and Dy doped Terbium manganite $TbMnO_3$ using CASTEP.
2) To determine and analyze the magnetic and electronic (Band structure, DOS, PDOS) properties of pure and Dy doped $TbMnO_3$.
3) To estimate the dielectric constant and optical properties for pure and Dy doped $TbMnO_3$ for Spintronic devices.

1.4 Scope of Study

- This work is carried out using numerical simulation coding to study pure and Dy doped $TbMnO_3$ structures in orthorhombic phase.
- The orthorhombic structure has developed in the CASTEP by using lattice parameters (a = 5.293 **Å,** b = 5.838 **Å**, c = 7.403 **Å).** The optimization of unit cell is carried out by adjusting cut-off energy 437.4 eV through GGA-PBE. K-mesh has been set 5×5×4 for Brillouin-zone sampling size. The minimum energy (-31480.3073 eV) obtained at the lattice parameters (a=5.299 **Å,** b= 5.809 **Å**, c= 7.415 **Å).**
- The optimized parameters are used to build 2×2×1 and 2×2×2 pure super cells and Dy dopants have been introduced in 2×2×2 super cell as monoatomic, diatomic, and triatomic doping concentration in pure TMO structure.
- The bond length, band structure, lattice parameters, density of states, bond population overlap, partial density of states, and dielectric function for pure and Dy-doped TMO material are calculated.

1.5 Significance of the Study:

The development of new potential material is aided by present study for Spintronic application at low temperature. This research will help us to understand that how the Dy dopant in $TbMnO_3$ material effect the electronic and magnetic properties specially magnetization and spin polarization.

CHAPTER 2

LITERATURE REVIEW

2.1 Introduction

This chapter compiles and summarizes the surveys from the academic journals, books, and other sources that are related to the field of the study including density functional theory (DFT), multiferroics and its types. This chapter starts with brief introduction of multiferroic material, classification of multiferroic, essential research literate survey for the research work. In this chapter, the magnetoelectric effect in $TbMnO_3$, technological application and effect of dopants in $TbMnO_3$ have also been discussed.

2.2 Spintronic RAM Technology

A magnetic field virtuously effect the switching mechanics of spintronic devices, and 99% of the energy used to write and read information during the switching process [15]. Furthermore, a significant amount of energy is required for the formation of electron-hole pairs in semiconductors during the switching process. Hence present technology switches 1-bit data with 10^{-11} J of energy [16], but this is significantly greater according to the Landauer limit which has a value of $E= K_BT \ln 2 \sim 3 \times 10^{-21}$ J/bit than lowest limit of computation switching energy [17].

For spin RAM technology, Intel, Berkeley and University of California have created a revolutionary switching process which is still in development by combining the material's ferroelectric and magnetoelectric capabilities [18]. However, it is challenging to increase RAM efficiency and lower switching energy due to high variety of materials with poor interconnectivity [19]. In Table 2.1 below, the values of different characteristics of spintronic RAM [20] are summarized.

Table 2.1: Different Parameters for Spintronic RAM

Symbol	**Quantity**	**Value**
ε (0)	Dielectric constant	10 < 52
M	Magnetization	25 < M < 500 MA/cm
P_s	Spin polarization	> 80%

In this field the other major task is to enhance the coupling between ferroelectric polarization and magnetization [21, 22]. Therefore, it is impossible to achieve optimal low-switching features by using a large variety of materials that also provide a heating factor. The only way to reduce the amount of multifunctional materials is to combine all switching abilities in a single phase [16]. Thus, finding a single multiferroic material with appropriate magnetoelectric switching properties is getting a lot of interest [22].

2.2.1: Spin Polarization in Materials at the Fermi Level

Certain materials exhibit different properties, displaying either semiconductivity or insulating properties in one spin channel, while demonstrating conductivity in the other spin channel. In the realm of spintronic RAM technology, these materials play a crucial role in producing spin polarization (P_s) at E_F, which may be harnessed to control the switching state to turn off and on [20, 23]. The switching process is mostly dependent on electrons at the E_F in both spin channels (up and down). Metals possess the equal amount of electrons E_F, whereas half-metals exhibit a discrepancy in the number of electrons. Based on the difference of electrons there are two ways to calculate the spin polarization E_F. It may also be define using DOS at E_F [24, 25] and formula is given below

$$P_s = \frac{\boldsymbol{g_n(E_F)_\uparrow - g_n(E_F)_\downarrow}}{\boldsymbol{g_n(E_F)_\uparrow + g_n(E_F)_\downarrow}} \tag{2.1}$$

where $g_n(E_F)_\uparrow$ and $g_n(E_F)_\downarrow$ are DOS in spin up and down channel at E_F respectively which is defined as tunneling DOS. At least one atom from transition metal like Ni, Co, Mn, or Fe is necessary for 100% spin polarization at the E_F or half metallicity. Combining the d-states and p-states of these transition metals and oxygen respectively produced a remarkable outcome which is important factor for spin polarization [24].

2.2.2: Magnetization (M) of Materials

Dirac postulated a direct correlation between the electron spin and the magnetic behavior of material. Two electrons having the same orientation of spin cannot occupy the same orbital is explained by Principle of Pauli Exclusion, and Hund's rule specifies that only one electron having the same spin should occupy each orbital [26]. Thus, Pauli Exclusion Principle describes the total magnetic moment (M_s) of an atom. [27]. For example, in transition metals the magnetism is caused by unpaired electrons of d orbital energy states. Thus, the total magnetic moment (M_s) per unit volume (Ω_o) defines the volume magnetism (M) of material [28].

$$M = \frac{M_s}{\Omega_o} \tag{2.2}$$

Here magnetic moment is measured in Bohr magneton (μ_B) where $1\mu_B$= 9.274 $x10^{-24}$ Am^2 and M is measured in Am^2.

2.3 Multiferroics Materials

Ferroic material is characterized by the presence of switchable and spontaneous internal orientation. The alignment of electron can switch in ferroelectrics, ferromagnetics and Ferro-elastics by a stress field, magnetic field, and electric field. multiferroic materials refers to the presence of two or more ferroic order in a single phase [29–34]. The traditional source of magnetic order is exchange interactions between magnetic dipoles that result from empty electron orbital shells. Electric order is produced by order of local electric dipoles. The atomic displacements ordered by strain give rise to elastic order. The coexistence of electric and magnetic order is particularly interesting because it combines features that may be used for transmission, processing, and storage of information This unique property permits the interaction of both magnetic and electric fields with magnetic and electric order. However, this property is exceedingly rare due to the presence of partially filled atomic orbitals, necessary for magnetic dipoles or moments, which often precludes the occurrence of local electric dipoles. These are typically related with the presence of either electron lone-pair configuration or an empty d-shells. It enables the interaction of both electric and magnetic order with the electric and magnetic fields. Nevertheless, this characteristic is extremely rare because of local electric dipoles which are usually connected to the presence of empty d-shells or configuration of an electron-lone pair [35]. Multiferroics gain huge attention for applications because of the conversion ability of charge to magnetic field and spin to charge. Magetoelctric coupling which enables control of ferroelectric polarization with the help of magnetic field and spin polarization by electric field is one of the interesting features of multiferroics. Two categories of multiferoic exist based on their respective features [36, 37].

2.3.1 Multiferroics Type-I

The ferroelectric and magnetic ordering in type-I multiferroics because of distinct mechanism do not occur at same temperatures which shows a weak coupling between two orders. Typically, the ferroelectric state manifests at a higher temperature, where the spontaneous polarization occur at a rate of 10-100 μC/cm^2. $BiFeO_3$ is a prominent example of extensively investigated type-I multiferroic [35].

2.3.2 Multiferroics Type-II

Magnetic order is the direct cause of the ferroelectricity in type-II multiferroic. This implies that there must be a strong coupling between these two orders. $TbMnO_3$ is an example of a type-II multiferroic where a spontaneous electric polarization is induces by a cycloidal antiferromagnetic ordering at ∼27 K. An applied magnetic field can frequently change the ferroelectric polarization of type-II multiferroics, or vice versa because of the material's strong coupling. The lower polarization magnitude (10^{-2} μC/cm^2) of type-II multiferroic is a practical limitation. Finding a material with both strong polarization of type-II multiferroics and electric polarization of Type-I multiferroics is one of main issues that's researchers are facing in the field of multiferroics [35].

2.4 Multiferroic Terbium Manganite

$TbMnO_3$ is a typical example of magnetoelectric multiferroics, which exhibits gigantic magnetoelectric response. According to neutron diffraction studies, the Mn moments in $TbMnO_3$ undergo an antiferromagnetic transition at $\mathbf{T_N}$ (∼41 K). Ferroelectric order gradually develops with decreasing temperature (T) down to $\mathbf{T_C}$ (∼26 K) when the spin structure transforms into a cycloidal spiral structure. Upon further decreases in T, Tb magnetic moment shows long-range ordering at T_{Tb} (∼7 K) [12].

Strong magnetoelectric coupling has shown in $TbMnO_3$. In an adiabatic process the temperature variation of magnetic materials is described by the magnetocaloric effect (MCE) resulting from the magnetic entropy shift under the influence of an external magnetic variation (ΔSm). Due to its captivating physical features The $TbMnO_3$ holds promise application in spintronics and can be utilized in magnetic refrigeration particularly at low temperature ranges. Under a constant magnetic field of 7T, a significant entropy change (ΔS = -18.0 J/Kg K) observed along the easy a-axis. In the magnetic field of 7 T, the associated refrigerant capacity (RCP) was found to be 309.7 J/Kg which has obtained close to the Tb^{3+} ordering temperature. Additionally, under 7T the $TbMnO_3$ rotation at 90° between a & b plane permits the change in entropy to maximize at about ΔS_{ba} = -8.2 J/Kg.K. Furthermore, a maximum change in entropy about ΔS_{ba} = -5.42 J/Kg.K has observed under the constant field of 7T when the $TbMnO_3$ crystal is rotated in the (ac) plane. This is significantly less than the entropy change that results from rotating the $TbMnO_3$ crystal in the (ab) plane along the a-axis [4]. Doping $TbMnO_3$ it with different elements such as iron (Fe), Cobalt (Co), Bismuth (Bi), Calcium (Ca), Tin (Sn), Titanium dioxide (TiO_2), Aluminum (Al), Lanthanum (La) and dysprosium (Dy), Gallium (Ga) are one of the attempts to improve the magnetic, electronic, and dielectric properties of TMO.

2.5 Magnetoelectric effect in $TbMnO_3$

Researchers by the year 2005 had identified robust magnetoelectric coupling in $DyMnO_3$ and $TbMnO_3$ in the applied magnetic field, while $GdMnO_3$ exhibit electric polarization [38, 39]. Subsequently, investigations were carried out to understand the features of the magnetic phase that generated the ferroelectric behavior in these substances. A single crystal TMO were investigated by Kenzelmann et al. with the help of Neutron diffraction experiments [40]. Figure 2.1(a) shows a sinusoidal magnetic order of the Mn^{3+} moments below 41 K, which is consistent with the model that Kimura et al. proposed [41]. However, contrary to previous assumptions, the magnetic phase below 27 K was found to be non-commensurate, dispelling the notion of an incommensurate-commensurate "lock-in" transition as the trigger for ferroelectricity. Instead, it was suggested that the phase exhibited a cycloidal pattern, with Mn3+ moments forming an ellipsoidal spiral in the b-c plane, as depicted in Figure 2.1(b). By analogy with the description for a similar effect in $Ni_3V_2O_8$, Kenzelmann et al. describe the presence of a ferroelectric order in TMO [42].

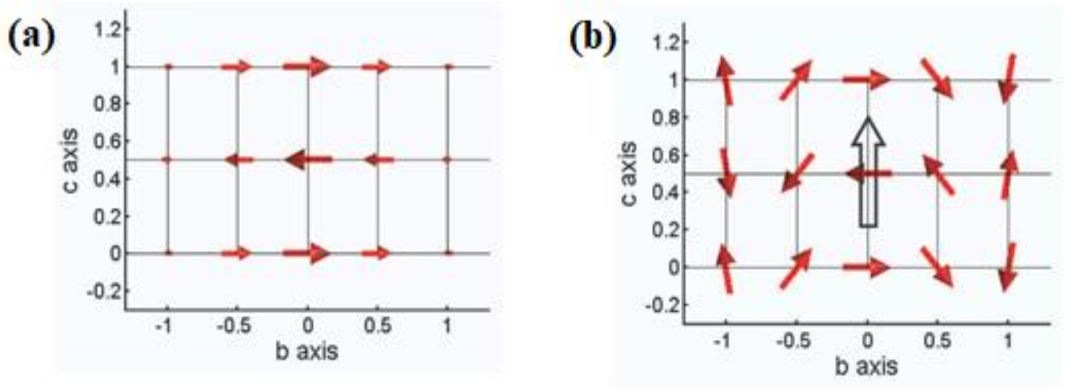

Figure 2.1: (a) The Mn sinusoidal magnetic order below 41 K and **(b)** in $TbMnO_3$, the cycloidal magnetic order below 27 K. The electric polarization in (b) is indicated by the black arrow [40]

For $TbMnO_3$ and $Ni_3V_2O_8$, the electric polarization's direction was accurately predicted by using symmetry arguments. In non-collinear magnets like $TbMnO_3$ for explaining the magnetoelectric coupling, Katsura et al. developed a microscopic model [43]. For neighbouring spins S_j and S_i separated by a r_{ij} vector, it was suggested that spin current $j_S \propto S_i \times S_j$ induced the electric polarization, , [44]

$$\mathbf{P} \propto \mathbf{r_{ij}} \times (\mathbf{S_i} \times \mathbf{S_j}) \qquad 2.3$$

2.7: Effect of dopants on Properties of TMO

Dopants play a very important role in tailoring the properties of multiferroic materials which influence their structural parameters, electronic structure, magnetic behavior, optical properties, and overall performance. Introducing different dopants, which are atoms or ions of different elements can modify the stability, conductivity and charge carriers' dynamics of multiferroic materials. Researchers can optimize multiferroic materials by strategically selecting and substituting dopants for specific applications. The effects of different dopants on the properties of $TbMnO_3$ are given in Table 2.2.

Table 2.2: The impact of dopants on multiferroic properties of $TbMnO_3$

Material	**Dopant**	**Synthesis Methods**	**Outcomes**	**Published Year**
$TbMnO_3$	Al	Conventional solid state reaction	A weak ferromagnetic behavior has shown by the doped samples	2007 [7]
$TbMnO_3$	Al	solid-state reaction	With the increasing Al content, an increase has observed in the magnetization	2012 [45]
$TbMnO_3$	Al	DC sputtering technique	for the Al^{3+} doped films magnetization saturation and remanence showed larger values	2019 [46]

Materials	**Dopant**	**Synthesis Methods**	**Outcomes**	**Published Year**
$TbMnO_3$	Fe	conventional solid-state reaction	with the increase in frequency dielectric dissipation peaks shifted to high temperature	2014 [9]
$TbMnO_3$	Fe	solid sintering method	with the increase in Fe content ($x \leq 0.5$) the activation energy of doped samples decreased while it increased with the increase in Fe content ($x > 0.5$)	2015 [47]
$TbMnO_3$	Fe	solid-state reaction	in the high temperature range the dielectric dissipation peaks reappear and the dielectric constant became larger ($\sim 10^3$)	2016 [10]
$TbMnO_3$	Fe	sol-gel method	A reduction in magnetization has observed in all samples with Fe content	2018 [8]
$TbMnO_3$	Ga	conventional solid-state reaction	The doped samples showed a large dielectric constant as compared to the pure TMO	2012 [48]
$TbMnO_3$	Si	conventional solid-state reaction	The dielectric characteristics of TbMnO3 are significantly altered by the addition of Si.	2013 [49]
$TbMnO_3$	Dy	sol gel technique	all samples showed interesting behavior of specific heat which exhibit transitions	2014 [50].
$TbMnO_3$	Dy	sol gel method	in the temperature range of 20–24 K all samples showed ferroelectric transition	2015 [51]
$TbMnO_3$	Bi	solid state reaction	with an activation energy of ~20 meV, dielectric relaxation has observed	2013 [11]

2.9: Density Functional Theory

Density-Functional-Theory (DFT) serves as a comprehensive framework for addressing the ground-state energy of electrons in multi-atom systems [52]. For a cost-effective alternative to Hartree-Fock calculations, DFT stands out as a valuable method in computational physics. This approach proves particularly useful for exploring the electronic characteristics of many-body systems through functional that spatially depend on electron density instead of wave-functions. Originating from the Thomas-Fermi model, which depicts an almost uniform distribution of electrons within an atom, DFT grapples with challenges related to energy exchange and tends to overlook electron correlation. The foundational principles of DFT trace back to the Hohenberg-Kohn theorems [53].

2.9.1: Many-Body Problem

A multicomponent system composed by A components is characterize by the non-relativistic time-independent Hamiltonian in the presence of external potentials $v_1(r), v_2(r), \ldots . v_A(r)$ which coupled to the densities $n_1(r), n_2(r), \ldots . n_A(r)$ of the different components is

$$\begin{aligned} \hat{H} &= \hat{T} + \hat{W} + \hat{V} \\ &= \sum_{\alpha=1}^{A} \int d^3r \hat{\psi}_\alpha^\dagger(r) \left(-\frac{1}{2m_\alpha} > \nabla^2\right) \hat{\psi}_\alpha(r) \\ &+ \frac{1}{2} \sum_{\alpha,\beta=1}^{A} \iint d^3r d^3r' \, \hat{\psi}_\alpha^\dagger(r) \hat{\psi}_\beta^\dagger(r') w_{\alpha,\beta}(r,r') \hat{\psi}_\beta(r') \hat{\psi}_\alpha(r) \\ &+ \sum_{\alpha=1}^{A} \int d^3r \hat{\psi}_\alpha^\dagger(r) v_\alpha(r) \hat{\psi}_\alpha(r) \end{aligned} \tag{2.4}$$

Where $\hat{\psi}_\alpha = \sum_{k\lambda} \phi_{k\lambda}(r) \hat{b}_{k\lambda\alpha}$ is representing a field operator, its Hermitian conjugate is representing by $\hat{\psi}_\alpha^\dagger(r)$; for a particle of the component α $\hat{b}_{k\lambda\alpha}$ is showing annihilation operator and some complete set of orthonormalized wavefunctions are representing by $\phi_{k\lambda}(r)$ is [54]. The potential that interacts a particle of component β at position r' and the component α at position r is $w_{\alpha,\beta}(r,r')$.

2.9.2: The Hohenberg-Kohn Theorem

For a bound system of interacting electrons, the Hohenberg-Kohn theorem is described by the Hamiltonian as follows: it is asserted that expectation value of any observable $\hat{O}$ in the ground state is a distinct functional solely determined by the specific electron density of the precise ground state

$$\left\langle \Psi[\mathrm{n(r)}] \mid \hat{O} \mid \Psi[\mathrm{n(r)}] \right\rangle = \mathrm{O}[\mathrm{n(r)}] \qquad 2.5$$

This theorem's proof is rather simple and may be found elsewhere. The variational nature of the energy functional is demonstrated by a second Hohenberg-Kohn theorem assertion.

$$E_{v_0}[n(r)] = \left\langle \Psi[\mathrm{n(r)}] \mid \hat{T} + \widehat{W} + \hat{V}_0 \mid \Psi[\mathrm{n(r)}] \right\rangle$$

$$= F_{HK}[n(r)] + \int d^3 r v_0(r) n(r) \qquad 2.6$$

With

$$F_{HK}[n(r)] = \left\langle \Psi[\mathrm{n(r)}] \mid \hat{T} + \widehat{W} \mid \Psi[\mathrm{n(r)}] \right\rangle \qquad 2.7$$

Where the ground state energy E_0 and ground state density $n_0(r)$ reflects the system's external potential $\hat{V}_O$. According to the Rayleigh-Ritz principle, the functional E_{v_0} possesses the following

$$E_0 = E_{v_0}[n_0(r)] < E_{v_0}[n(r)] \qquad 2.8$$

Then by minimizing thefunctional $E_{v_0}[n(r)]$ we may determine the precise ground state energy

$$E_0 = \min_{n \in \mathcal{N}} E_{v_0}[n(r)] \qquad 2.9$$

The challenge of determining the lowest energy state with respect to the wave function, represented by the set of ground states densities $\boldsymbol{\mathcal{N}}$ has been reformulated as the more straightforward task of identifying the minimum of the functional concerning the three-dimensional trial function $n(r)$. While this shift simplifies the problem, the central issue persists in constructing the precise functional F_{HK} or a least, devising an effective approximation for it [54].

2.9.3: Kohn-Sham Equation

According to the Hohenberg-Kohn theorem, if a system with N non-interacting electrons is examined, the energy functional for this system is

$$E_s[n(r)] = T_s[n(r)] + \int d^3r v_s(r) n(r) \qquad 2.10$$

The symbol $T_s[n(r)]$ represents the kinetic energy functional associated with non-interacting electrons. In the case of this system, solving the variational equation $\delta E_s[n(r)] = 0$ provides the accurate ground state density $n_s(r)$ for the non-interacting system [54].

The fundamental assertion in establishing the Kohn-Sham equations is that for interacting system, there exist a local single-particle potential $v_s(r)$ for which the interacting system's ground state density $n(r)$ equals the non-interacting system's ground state density $(n(r) = n_s(r))$.

Revisiting the challenge involving the electrons interaction with an external potential $v_0(r)$ and ground state density n_0(r), we can represent the total energy functional of the interacting electrons as a function of the kinetic energy functional of the non-interacting electrons as follows

$$E_{v_0}[n(r)] = T_s[n(r)] + \int d^3r v_0(r) n(r)$$

$$+\frac{1}{2}\iint d^3r d^3r' \frac{n(r)n(r')}{|r-r'|} + E_{xc}[n(r)] \qquad 2.11$$

Where the exchange-correlation functional $E_{xc}[n(r)]$ is defined as

$$E_{xc}[n(r)] = F_{HK}[n(r)] + \int d^3r d^3r' \frac{n(r)n(r')}{| r - r' |} - T_s[n(r)] \qquad 2.12$$

For interacting electrons, the Euler-Lagrange equations associated with the energy functional are as follows

$$\delta E_{v_0}[n(r)] = \int \delta n(r)\{\frac{\delta T_s[n(r)]}{\delta n(r)} \mid_{n(r)=n_0(r)} + v_{eff}(r) - \epsilon\} = 0 \qquad 2.13$$

Where

$$v_{eff}(r) = v_0(r) + \int d^3r' \frac{n_0(r')}{\mid r - r' \mid} + v_{xc}[n_0; r] \qquad 2.14$$

And

$$v_{xc}[n_0; r] = \frac{\delta E_{xc}[n(r)]}{\delta n(r)} \mid_{n(r)=n_0(r)} \qquad 2.15$$

Here, the symbol ϵ serves as a Lagrange multiplier, introduced to ensure the conservation of particles. Subsequently, the task of minimizing the density function, denoted as n(r), involves solving the single particle equation

$$\left(-\frac{1}{2}\nabla^2 + v_{eff}(r) - \epsilon_i\right)\varphi_i = 0 \qquad 2.16$$

With

$$n_0(r) = \sum_{i=1}^{N} \mid \varphi_i(r) \mid^2 \qquad 2.17$$

and

$$v_{eff}(r) = v_0(r) + \int d^3r' \frac{n_0(r')}{\mid r - r' \mid} + v_{xc}[n_0; r] \qquad 2.18$$

The system of equations denoted as (2.16) -(2.18) constitutes the Kohn-Sham equations. Since the single-particle potential depends on the density, the complete set of equations must be solved again in a self-consistent manner [54].

The ground state energy is giving by

$$E_0 = \sum_i \epsilon_i - \frac{1}{2}\iint d^3r d^3r' \frac{n(r)n(r')}{\mid r - r' \mid} + E_{xc}[n] - \int d^3r\, v_{xc}(r) \qquad 2.19$$

in theory all the many-body effects are included if the functional forms for E_{xc} (exchange-correlation energy) and v_{xc} (exchange-correlation potential) are precisely known. The practical advancement of Density Functional Theory (DFT) hinges entirely on the ability to discover approximations for the exchange-correlation energy E_{xc} that strike a balance between simplicity and accuracy.

2.9.4: The Local Density Approximation

The widely employed functional known as the Local Density Approximation (LDA) is a simple yet pivotal method for calculating exchange-correlational energy, with the local density serving as a crucial parameter in this process. In LDA, the homogeneous gas model is utilized to assess all system parameters, grounding its foundation on the exchange-correlation energy of the uniform electron gas. This particular energy computation takes into account the gradual changes in charge density occurring on an atomic scale.

It is noteworthy that the functional E_{xc} is not precisely known, leading to the utilization of various approximations in the fields of atomic, molecular, and solid-state physics. Among these approximations, LDA stands out as the most widely adopted. LDA is specifically defined by its reliance on the exchange-correlation energy of the uniform electron gas and its ability to accommodate slow changes in charge density at the atomic scale.

$$E_{xc}^{LDA} = \int d^3r e_{xc}^{hom}(n_0)\big|_{n_0 \to n(r)} \qquad 2.20$$

The local density approximation (LDA) involves substituting the constant density n_0 by the local density $n(r)$ in the exchange-correlation energy per particle $e_{xc}^{hom}(n_0)\big|_{n_0 \to n(r)}$ of a homogeneous electron gas. In essence, LDA approximates the exchange-correlation energy density at each point r in a spatially inhomogeneous system by considering a homogeneous electron gas whose density matches the local n_0 [54].

2.9.5: The Generalized Gradient Approximation

A refined version of LDA involves the introduction of the generalized gradient approximation (GGA). This enhancement entails expressing the exchange-correlation energy by incorporating densities and their respective local gradients.

$$E_{xc}^{GGA} = \int d^3 r e_{xc}^{GGA}(n, \nabla n) \qquad 2.21$$

The determination of the $e_{xc}^{GGA}(n, \nabla n)$ lacks a unique definition, leading to the proposal of various forms. These formulations are constructed employing asymptotic behavior of effective potentials, sum rules, general scaling characteristics, and other relevant considerations. In our computations, we adopted the GGAs put forth by Perdew, Burke, and Ernzerhof, as well as Perdew and Wang 91.

The GGA exhibits significant advantages, most notably that it performs better than the LDA when calculating properties like bond dissociation energies. The LDA may overestimate these energies by up to 100%, whereas the GGA typically yields errors of approximately 10% or less. Additionally, the GGA consistently demonstrates improved accuracy compared to the LDA in determining the bulk modulus of solids, boasting an error rate of around 10%, in contrast to the LDA's approximately 20% error rate.

CHAPTER 3

METHODOLOGY

3.1 Introduction

The methods, materials, and software programs used for the numerical simulation of pure and doped Terbium Manganese Oxide ($TbMnO_3$) are described in this chapter. First-principles calculations are performed using different coding programs such as Quantum espresso, CASTEP, Wien2K, DFTB+ and VASP. The accuracy of these programs towards the compuTable properties is different but these coding provide a plausible route for experimental study [55, 56]. CASTEP has high accuracy and applies electron density multistage to estimate coulomb potential in the solid state material [57]. The CASTEP has advantage over other coding programs due to the independency of atomic positions and no basis set suppression error (BSSE) effect [58]. In this research work, CASTEP coding was used to study the optical, electronic, structural, and magnetic properties of $TbMnO_3$. The simulation methods utilizing the CASTEP module for performing DFT calculations, along with its working are discussed in this chapter. A brief description of the numerical simulation and associated parameters of the systems has also been explained.

3.2 Cambridge Serial Total Energy Package (CASTEP)

A specially designed coding program based on quantum mechanics known as CASTEP software which is used to study solid state of matter. In this software, plane-wave pseudopotential, and density functional theory (DFT) are included to perform first-principles quantum mechanics calculations. Surface properties and crystal structure of solid materials are determined based on these calculations. Studies of different properties are often including coding package for typical applications like band structure, structural properties, optical properties, surface chemistry, and density of states. The investigation of spatial distribution of wave functions and charge density in solid material is another use of CASTEP [36, 59].

The CASTEP module from BIOVIA Materials Studio 2020 is used in this research work to calculate different properties using a plane wave (PW) basis set. By the examination of molecular and atomic structures, as well as the behavior and properties of materials in mechanical engineering and materials science, CASTEP serves as an extensive modeling and simulation tool. It helps researchers to create new materials. Now a days, Materials Studio is used by engineers and researchers to produce a wide range of well behaving materials such as nanomaterials, catalysts, fuel cells, polymers, pharmaceuticals, composites, polymers, battery materials, alloys, metals, and more [36, 59].

3.2.1 Exchange-Correlation Function

Within the CASTEP module, different non-local and local exchange correlation functions including generalized gradient approximation (GGA-PBE), local density approximation (LDA CA-PZ), and hybrid functions are employed for computing electron-electron interaction. Hartree–Fock (HF) calculations, while tending to overestimate band gap values and being time-consuming, are often utilized. Although hybrid methods yield band gaps approximating experimental data, their significant drawback lies in the inaccurate treatment of d-electrons, making them unsuitable for addressing p-d and s-d electron repulsion. The GGA approach, while underestimating band gaps, proves more useful for exploring various properties of energetic supercells without energy minimization. CASTEP's local representation of the exchange-correlation potential stands out as one of the most accurate descriptions available. The accuracy of structures and predicted energies can be improved by Gradient-corrected calculations. Notably, the Perdew-Burke-Ernzerhof correlations (PBE) and Perdew-Wang generalized-gradient approximation (PW91) play a crucial role in improving calculation accuracy [60].

3.2.2 Pseudopotentials

Pseudopotential theory is employed to examine electron-ion interactions, utilizing pseudopotentials to represent nuclei and core electrons. This approximation, categorized as either soft pseudopotentials or hard pseudopotentials based on the quantity of Fourier components used, minimally impacts inter-atomic interactions. Within CASTEP, four types of pseudopotentials [60] are available: i) on-the-fly generated (OTFG) ultrasoft, ii) ultrasoft (USP), iii) norm conserving (NCP), and iv) on-the-fly generated (OTFG) norm conserving. Ultrasoft pseudopotentials, known for their accuracy and efficiency, typically require lower cutoff energy and less computation time compared to NCP. The stiffness of a pseudopotential is a key concept, classified as soft when fewer Fourier components are needed for precise representation and hard otherwise. Early norm-conserving pseudopotentials for transition metals were notably hard, but advancements in new generation methods have introduced softer pseudopotentials with a broader range of values. Various schemes proposed in the literature have enhanced the convergence properties of norm-conserving pseudopotentials. [60].

3.2.3 Self-consistent Electron Minimization

CASTEP offers various electronic relaxation options, with the default and most efficient method relying on density mixing. Instead of pursuing self-consistent minimization of total energy, the sum of electronic eigenvalues is minimizing using this method within a constant potential. Following minimization, the initial density undergoes mixing with the new charge density, and this iterative process continues until system convergence is achieved. CASTEP also accommodates a more traditional approach involving total energy minimization for electronics, where electronic wave functions are expanded using a plane-wave basis set and adjusted to minimize total energy. Additionally, CASTEP supports an all-bands method that facilitates energy minimization with automatic updates for all wave functions. A preconditioned conjugate gradient method is used in this specific scheme [60].

3.3 Numerical & Simulation Details

This section provides a comprehensive overview of the materials, methodology, and numerical procedures employed for simulating pure and Dy doped $TbMnO_3$ with the help of CASTEP. The process is segmented into three components, encompassing construction and optimization, the computation of electronic behavior, and the determination of optical behavior. Subsequent sections furnish in-depth details on each of these aspects.

3.3.1 Construction & Geometry Optimization of $TbMnO_3$

$TbMnO_3$ adopts a Pbnm symmetric orthorhombic distorted perovskite structure. This structure comprises corner-sharing MnO_6 octahedra, where the Mn ions positioned at the center of each octahedron [61–63]. Tb and Mn atoms exclusively occupy a single in-equivalent site each within the crystal structure, specifically at sites 4c and 4b, respectively. Additionally, there are two distinct oxygen sites, namely 4b for two apical O1 atoms and 8d for four planar O2 atoms [63] as shown in Figure 3.1. The (Tb, A) ions occupy the central positions within a cube constituted by MnO6 octahedra. This arrangement exhibits significant distortion, primarily due to the disparity in (Tb, A)-O and Mn-O bond distances, along with the Jahn-Teller (JT) distortion affecting the Mn-O bonds [4][61].

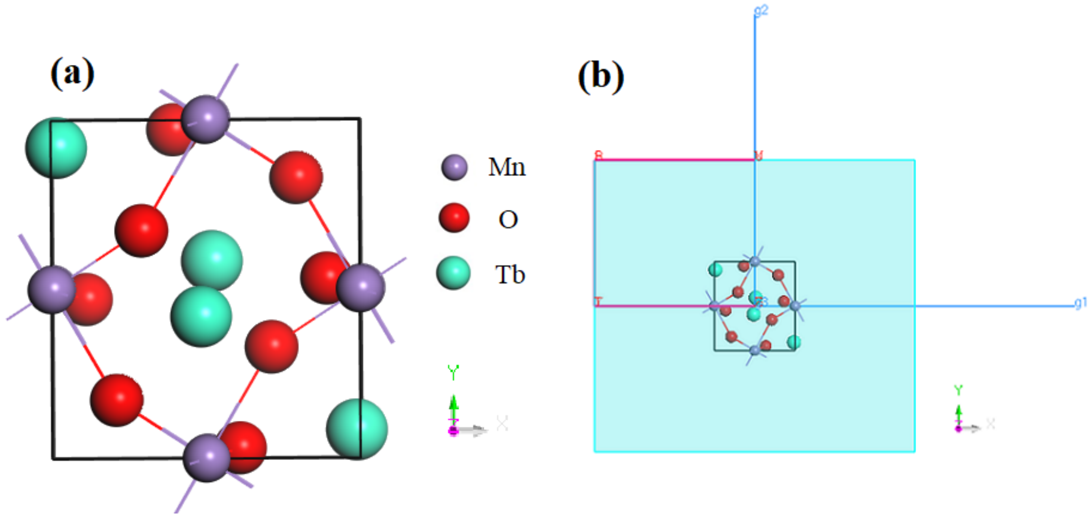

Figure 3.1: (a) Pure TbMnO$_3$ Unit cell **(b)** Brillouin-zone Structure of pure unit cell

The orthorhombic phase (crystal structures) of TbMnO$_3$ unit cell was built in CASTEP as shown in Figure 3.1 using the reported Pbnm space group [4, 11, 44, 61–65], lattice parameters **(a = 5.293 Å, b = 5.838 Å** and **c = 7.403 Å, $\alpha = \beta = \gamma = 90^o$)** [7, 44, 63, 64] and atomic positions [4] as listed in Table 3.1. The basis set was constructed using a plane wave function with a cutoff energy of 437.4 eV and the K-points meshes (MP-Grid size) was set as 2×2×1 [63].

Table 3.1: Reported Atomic Positions of TbMnO$_3$

Atom	**Atomic Positions**			**Wyckoff Positions**
	X	**Y**	**Z**	
Tb	0.9836	0.081	0.25	4c
Mn	0.5	0	0	4b
O1	0.1083	0.4694	0.25	4b
O2	0.7085	0.3267	0.0523	8d

For geometry optimization, calculations were performed through GGA-PBE along with OTFG ultrasoft pseudopotential [4, 44, 61–64]. For spin-polarized calculations, Hubbard Potential (U) was used in the DFT+U [4, 61, 63]. Hubbard effective parameter

U was varied between 0 and 7 eV to obtain the band gap close to the experimental value.

The Hubbard-U was employed to reproduce the electronic structure for the localized electron states particularly those bands which derived from electrons of Mn 3d state. The Hubbard U = 6 eV on 4f-Tb and U = 2.5 eV for 3d-Mn states were opted. The correction of 3d-Mn states was kept constant (U (Mn) = 2, 3, 4 eV) to optimize the U corrections for Mn and Tb, while for each fixed value of Mn, the correction of 4f-Tb states was varied (U (Tb) = 4, 5, 6, 7, 8, 9, 10 eV). The utilization of the Hubbard potential (U) was applied to localize the 4f states, leading to improvements in both the band-gap value and the magnetic moment [4, 61, 63, 66].

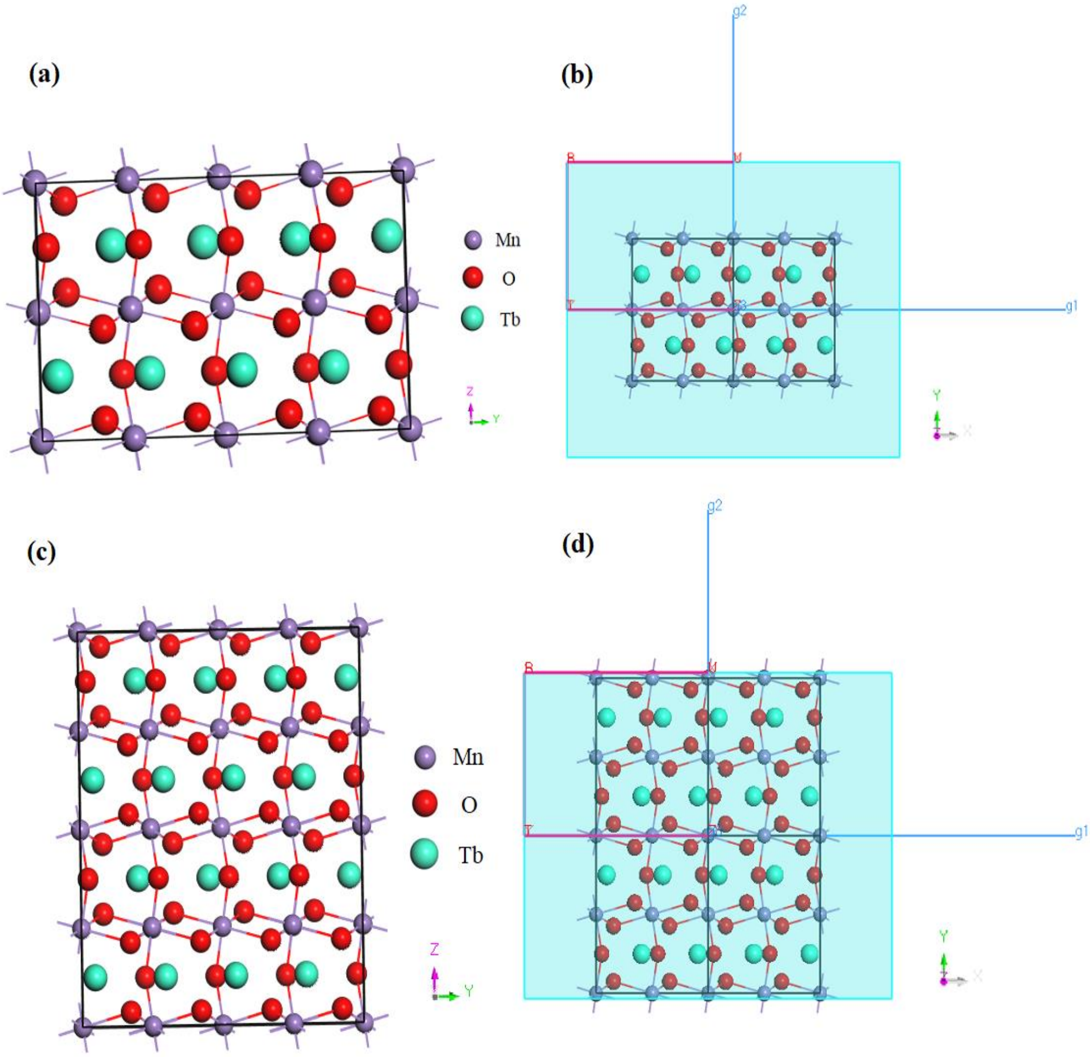

Figure 3.2: (a) Pure $TbMnO_3$ (2×2×1) **(b)** Brillouin-zone Structure of 2×2×1 TMO **(c)** Pure $TbMnO_3$ (2×2×2) **(d)** Brillouin-zone Structure of 2×2×2 TMO

Geometry Optimization tolerance values were adjusted accordingly as listed in Table 3.2 and the tolerance in the self-consistent field (SCF) calculation were set 1.0×10^{-5} eV/atom [63]. By applying zero external stress, Limited memory Broyden–Fletcher–Goldfarb–Shanno (LBFGS) algorithm was employed with line research approach.

Table 3.2: Geometry Optimization Convergence Tolerance Values

Quality	**Energy (eV/atom)**	**Force (eV/ Å)**	**Stress (GPa)**	**Displacement (Å)**
Coarse	5.0×10^{-5}	0.1	0.2	0.005

The optimized lattice parameters were used to construct 2×2×1 and 2×2×2 supercell for pure Terbium Manganite ($TbMnO_3$) as shown in Figure 3.2. To study the effect of doping in $TbMnO_3$, the Tb atoms were replaced with the Dy atoms in 2×2×2 super cell up to 3 numbers of atoms as shown in Figure 3.3. Geometry optimization of doped structures was carried out without applying Hubbard (DFT+U) and fixed occupancy was unchecked. Brillouin-zone K-mesh was set 5×5×4 for pure unit and supercell calculations. For doped supercell of TMO, brillouin-zone K-mesh (MP-Grid size) was set 1×1×1.

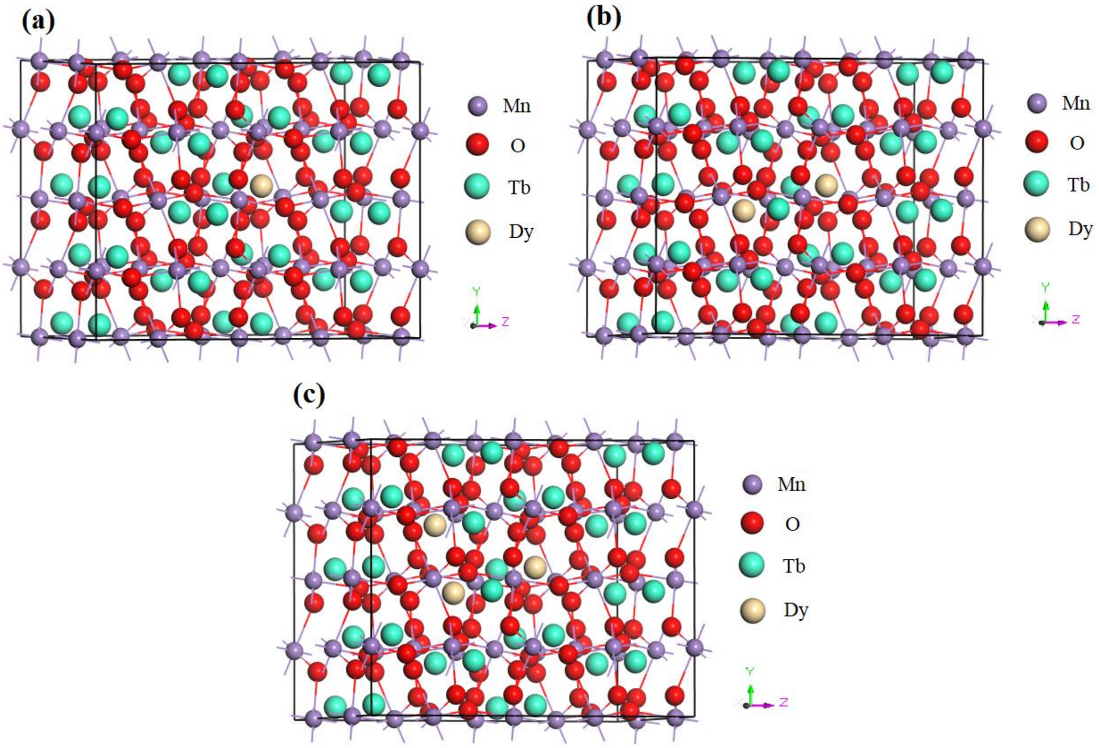

Figure 3.3: (a) 1-Dy doped TMO **(b)** 2-Dy doped TMO 2 **(c)** 3-Dy doped TMO

3.3.2 Calculation of Electronic and Magnetic Properties

The value of k points and SCF convergence was adjusted as 5×5×4 and 1.0×10^{-5} eV/atom, respectively. Formal spin was adjusted as the initial spin value to determine the energy and spin polarized values. To calculate magnetic properties population analysis was checked. The GGA-PBE plane wave function was employed, with a cutoff energy of 437.4 eV, to find the maximum and minimum energy values. During calculations higher values were ignored obtained from the pseudopotentials Tb (549.7), O (571.4eV), Mn (519.7). The spin-based DOS, spin magnetic moment, spin-based PDOS, spin polarization at E_F and volume magnetization for pure and Dy doped TMO has calculated using equation 2.1 and 2.2.

3.3.3 Calculation of Optical Properties

The optical characteristics of both pure and Dy doped $TbMnO_3$ were analyzed to investigate the material's suitability for various devices and applications. By calculating the complex-dielectric function, the optical characteristics were determined. This study involved the calculation of various optical properties including excitation coefficient $K(\omega)$, refractive-index $n(\omega)$, reflectivity $R(\omega)$, loss function $L(\omega)$, complex-dielectric-function $\varepsilon(\omega)$, and absorption-coefficient $\alpha(\omega)$ for pure and Dy doped TMO. These calculations were performed in CASTEP and Equations 3.1 to 3.6 were used to calculate these optical properties [67, 68].

Dielectric Function

$$\varepsilon(\omega) = \varepsilon_1 + i\varepsilon_2 \qquad 3.1$$

Where ω is the frequency, ε_1 presents the real part and ε_2 presents the imaginary part.

Refractive index

$$n(\omega) = \frac{1}{\sqrt{2}}\{[\varepsilon_1^2(\omega) + \varepsilon_2^2(\omega)]^{\frac{1}{2}} + \varepsilon_1^2(\omega)\}^{\frac{1}{2}} \qquad 3.2$$

Where $n(\omega)$ is the refractive index which depend on angular frequency(ω), ε_1 is real part of dielectric function and ε_2 represents imaginary part.

Excitation constant

$$K(\omega) = \frac{1}{\sqrt{2}}\{[\varepsilon_1^2(\omega) + \varepsilon_2^2(\omega)]^{\frac{1}{2}} - \varepsilon_1^2(\omega)\}^{\frac{1}{2}} \qquad 3.3$$

Where $K(\omega)$ is the excitation constant, ε_1 represent real part of dielectric function and ε_2 denote imaginary part, and ω is representing the angular frequency.

Reflectivity

$$R(\omega) = \left| \frac{\sqrt{\varepsilon_1(\omega)+i\varepsilon_2(\omega)}-1}{\sqrt{\varepsilon_1(\omega)+i\varepsilon_2(\omega)}+1} \right| \qquad 3.4$$

Where $R(\omega)$ is the relectivity, ε_1 and ε_2 are the real and imaginary part of dielectric constants, and ω is the angular frequency.

Loss function

$$L(\omega) = \mathrm{Img}\left(\frac{-1}{\varepsilon(\omega)}\right) \qquad 3.5$$

Where $L(\omega)$ is the loss function which is the function of angular frequency ω, and it represent the imaginary part of dielectric constant(ε).

Absorption coefficient

$$A(\omega) = \frac{2\omega}{c}\mathrm{k}\alpha \qquad 3.6$$

Where α is the absorption coefficient, k is the extinction coefficient and ω is angular frequency.

3.4 Flow Chart

Figure 3.4 illustrates the sequential process employed for the theoretical examination of the structural, optical and electronic characteristics of pure and doped $TbMnO_3$. In first stage, the $TbMnO_3$ unit cell for orthorhombic phase was built with reported parameters. 10 optimized calculations were performed through GGA-PBE with OTFG ultrasoft pseudopotential. Spin polarized geometry optimization along with DFT+U was conducted, where the cut-off energy was adjusted to 437.4 eV for the maximum of 100 iterations while the basis quality was maintained at a fixed level, with hard compressibility settings employed specifically for transition metals. 2×2×1 and 2×2×2 super cells were constructed by using the most optimized lattice constants. 2×2×2 super cell was further optimized for monoatomic, diatomic, and triatomic doping concentration of Dysprosium (Dy) atom. The electronic properties, including DOS, band structure and PDOS, optical properties including extinction-coefficient, reflectivity, complex-dielectric-function, refractive-index, loss function and absorption coefficient and spin polarization were calculated following the introduction of impurity atom (Dy) and subsequent geometry optimization.

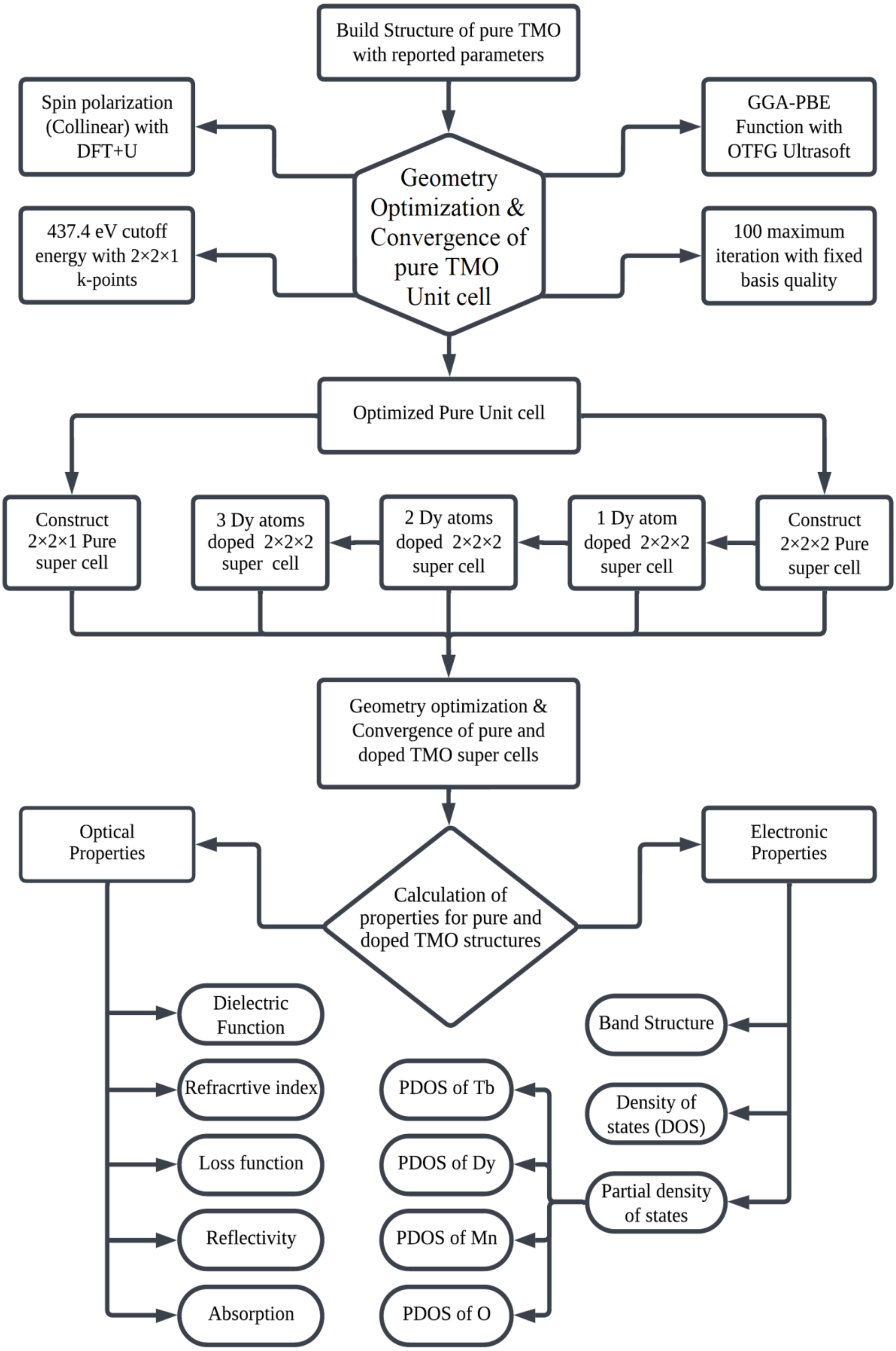

Figure 3.4: Flow chart of CASTEP methodology for numerical simulation of pure and Dy doped TMO

CHAPTER 4

RESULTS

4.1 Introduction

The results of theoretical treatment of both pure and Dy-doped $TbMnO_3$ (TMO) are presented in this chapter. This study presents the optical characteristics, band structures, density of state, optimized cell volume, partial density of state, dielectric constant, and equilibrium lattice constants for 2×2×2 pure and Dy-doped $TbMnO_3$ super cells in the orthorhombic phase.

4.2: Structural analysis

DFT analysis was used to study the different structural parameters of pure and doped TMO in orthorhombic phase. Structural variation in the cell volumes, lattice constants, bond distances, and bond lengths of TMO has been determined by substituting different number of Dy atoms as dopant.

4.2.1 Geometric optimization

The crystal structure of pure $TbMnO_3$ was built in CASTEP with 20 atoms per unit cell on orthorhombic phase. Geometry optimization was carried out to reduce the external stress and to minimize the total energy of the cell by changing its lattice. Total 10 geometry optimization calculations were performed by changing the lattice parameters gradually for ***a=5.291 Å to 5.303 Å, b=5.800 Å to 5.854 Å and c= 7.400 Å to 7.421 Å*** (***a≠b≠c,***). The total energy was calculated as a function of the unit cell volume to determine the optimized lattice using GGA approximation. The geometric optimization was performed using reported values and the comparison between experimental and theoretical data has been listed in Table 4.1. The results show that the calculated optimized lattice parameters are consistent with the reported value.

Table 4.1: Experimental & Optimized lattice parameters for orthorhombic $TbMnO_3$

Lattice Parameters	***a*** **(Å)**	***b*** **(Å)**	***c*** **(Å)**	**Volume**
Experimental Values [69]	5.293	5.838	7.403	228.7567 A^3 [49]
Optimized values (Present work)	5.299	5.809	7.415	228.2477 A^3

Values of reported lattice constants [49, 69] were used as starting values, while the overall energy was minimized relative to the unit cell volume. The graph was plotted between the total energy and unit cell volume for $TbMnO_3$ compound as presented in

Figure 4.1. The minimum energy (-31480.3073 eV) has been obtained for the lattice parameters (*a*=5.299 **Å,** *b*= 5.809 **Å**, *c*= 7.415 **Å).**

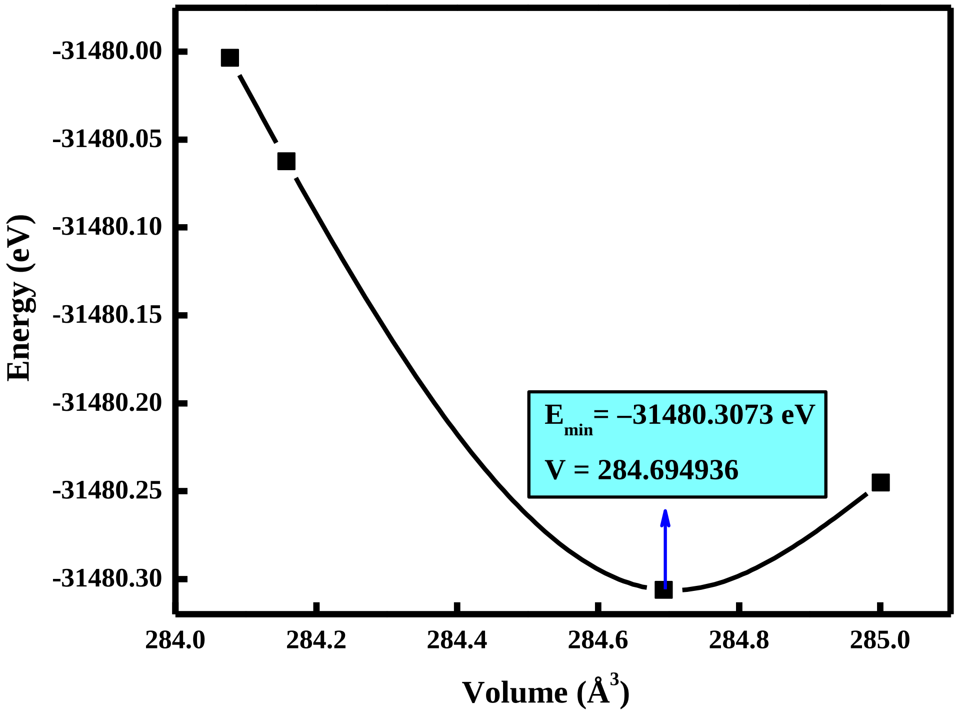

Figure 4.1: Total energy vs final volume for $TbMnO_3$ Unit cell

Optimized unit cell was changed into 2×2×1 and 2×2×2 pure super cells and then Dy dopant was introduce into 2×2×2 $TbMnO_3$ super cell as monoatomic, diatomic, and triatomic doping concentration in pure TMO structure. The geometry optimization of pure and doped super cells was performed to reduce the external stress before performing calculations for different electronic, magnetic and optical properties.

4.2.2 Crystal Structure

The lattice constants have been changed after addition of Dy impurities in TMO structure. The changes in the lattice constants and final volumes with corresponding Dy concentration are given in Table 4.2. The presence of doping atoms causes a variation in lattice parameters, which can be understood by the ionic size mismatch between the dopant (Dy) and host (Tb) atoms [61]. The lattice parameters “a” is decreased continuously, “b” is decreased up to second doping [50, 51, 70] whereas the lattice parameter “c” is increased with increase in number of dopant atoms [8, 47, 65, 70].

Table 4.2: Optimized lattice constants & cell volumes of pure and doped $TbMnO_3$

$TbMnO_3$ Structure	**Lattice Parameters**						**Final Volume (Å^3)**
	α	**β**	**γ**	**a (Å)**	**b (Å)**	**c (Å)**	
Pure	90°	90°	90°	6.292	7.919	5.714	284.708
1-Dy doped	89.9°	90°	89.8°	5.535	6.311	7.396	258.376
2-Dy doped	89.4°	89.9°	89.3°	5.510	6.256	7.469	257.439
3-Dy doped	89.8°	90°	89.7°	5.475	6.268	7.478	256.536

The bond angles and bond distances between Mn-O of pure and doped TMO are given in Table 4.3. The bond lengths and angles vary with the increase in the number of Dy atoms in TMO structure. Where $d_{1(Mn\text{-}O1)}$ is the average bond length/distance between Mn-O1, $d_{2(Mn\text{-}O2)}$ and $d_{3(Mn\text{-}O2)}$ are the average distance between Mn-O2.

Table 4.3: Bond distance & angle b/w Mn-O atoms of Pure and Doped $TbMnO_3$

$TbMnO_3$ Materials		**Distance (Å)**			**Bond angle (degree)**	
		$d_{1(Mn\text{-}O1)}$	**$d_{2(Mn\text{-}O2)}$**	**$d_{3(Mn\text{-}O2)}$**	**Mn-O2-Mn**	**Mn-O1-Mn**
Pure	**Exp** [65, 71]	1.946	2.243	1.889	145.70	143.98
	(this work)	2.153	2.546	2.009	137.488	133.719
1-Dy doped		1.981	2.518	1.918	143.338	137.566
2-Dy doped		1.993	2.386	1.972	147.247	138.597
3-Dy doped		2.010	2.462	1.921	143.454	137.305

4.3.1: Spin-polarized band structure and density of states

One of the most important areas of solid-state physics is the study of electronic structure since it provides an explanation for different features of material, including magnetic and optoelectronic capabilities, electronic conductivity, and heat capacity. Significant information of electronic properties can be collected from the density of states and partial density of states. The observed energy band structure at E_F for pure and doped $TbMnO_3$ are shown in Figure 4.3 (a) and (b) in which the K points are taken along x-axis and energy along y-axis.

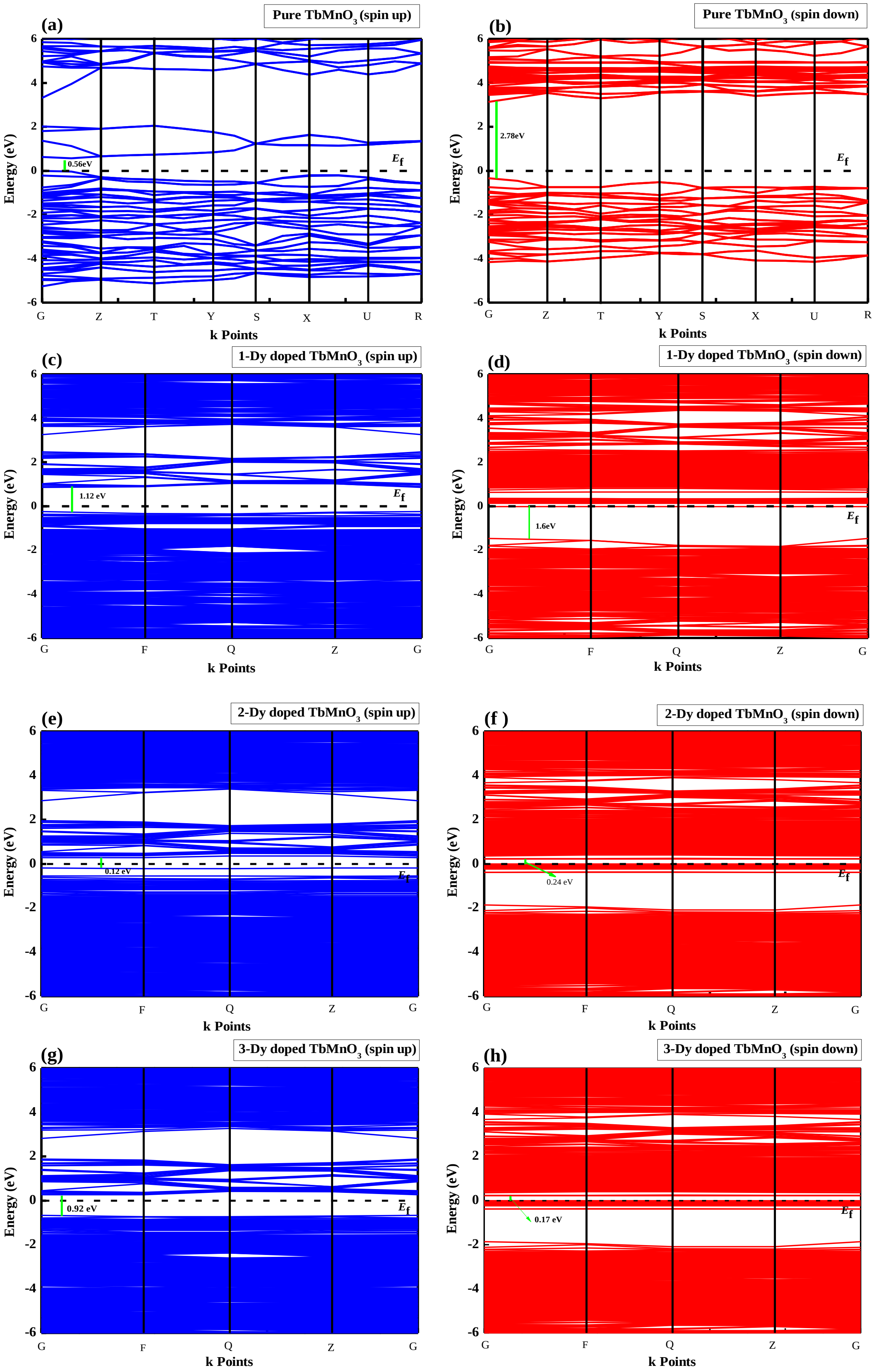

Figure 4.2: Calculated electronic band structure of pure and Dy-doped TbMnO3

Along the G-Z-T-Y-S-X-U-R direction, the energy band structures are computed for the highest number of symmetry points found in the Brillouin zone. [44]. The electronic band structure covers a wide range of energy levels from -6 eV to 6 eV. The spin up band gap of 0.56 eV has observed for pure $TbMnO_3$ which is in consistent with the reported experimental (0.489 eV) [72] and theoretical (0.55 eV) [4, 61] values, and spin down band gap at G point 2.78 eV has observed for pure $TbMnO_3$.

The band structures of TMO with the different number of Dy dopants are shown in Figure 4.2 (c to h) for both spin up and down. In doped $TbMnO_3$, both spin up and down band structures have shown direct band gap at the G point. The spin up band gap of 1-Dy doped $TbMnO_3$ is 1.12 eV and for spin down is about 1.6 eV. In 2-Dy doped $TbMnO_3$ structure the spin up band gap is about 0.12 eV whereas spin down band gap 0.24 eV is observed. In 3-Dy doped $TbMnO_3$ structure the spin up band gap 0.92 eV and spin down band gap 0.17 eV is observed.

Table 4.4: The band gaps of pure and doped $TbMnO_3$

Structures	**Band gap (spin up)**	**Band gap (spin down)**
Pure $TbMnO_3$	0.56 eV	2.78 eV
1-Dy doped	1.12 eV	1.6 eV
2-Dy doped	0.12 eV	0.24 eV
3-Dy doped	0.92 eV	0.17 eV

The variations in the band gap of pure and doped $TbMnO_3$ are listed in Table 4.4. The spin-up band gap initially increased upon the introduction of the first dopant, but subsequently decreased with the addition of a second Dy dopant. But the spin-down band gap consistently reducing with increasing Dy content. The individual contributions of atoms to bonding, anti-bonding states, conductivity, magnetic order, optoelectronic properties, and various other electronic and optical characteristics in crystalline solids are directly related to the structure of the Density of States. The electronic band structure, the total density of states for both pure and Dy-doped $TbMnO_3$ has been computed, as shown in Figure 4.3. A vertical line denotes the Fermi level (E_F), which serves as the boundary between bonding and anti-bonding states. The spin-down states in the conduction band shift closer to E_F, while the spin-up states in the valence band extend within the range of -2 eV to -7 eV.

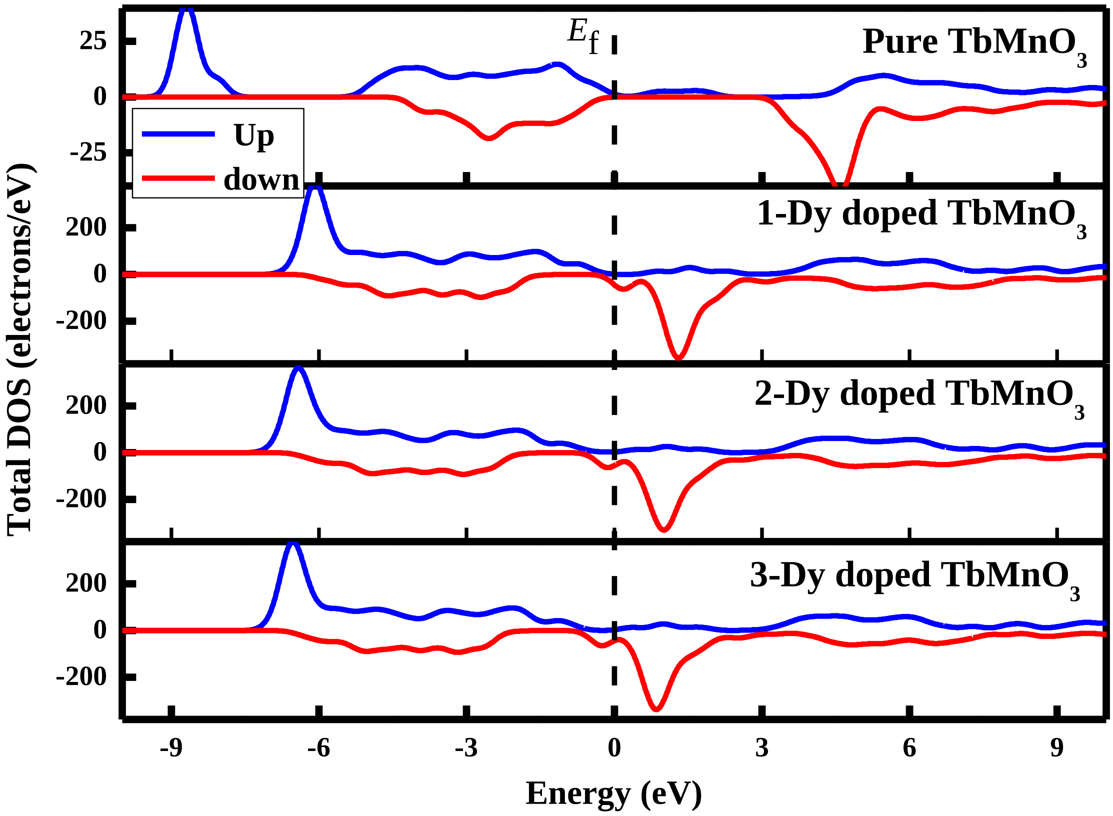

Figure 4.3: Comparison of total DOS for pure and doped $TbMnO_3$

The partial density of states for Tb, Dy, Mn, and O elements are also calculated as shown in Figure 4.4. Combining the band structure with the (partial) density of states, it has been observed that the spin up VB is dominated by Mn 3d (spin up) mixed with O 2P (spin up) and [44] above the Fermi level, the spin up CB is dominated by Tb 5d (spin up) states in the range of 3.04 eV to 5.6 eV [44]. The spin down CB is dominated by Tb 4f (spin down) states mixed with Mn 3d (spin down) states and spin down VB is dominated by Tb 4f (spin down) states mixed with O 2p (spin down) states. Furthermore, the width and PDOS for O 2p (spin up) states and Mn 3d (spin up) states are more prominent in the upper region of spin up VB than that for Tb 4f states, suggesting that Mn–O hybridization is stronger than Tb–O hybridization [44]. Ferroelectric polarization is significantly influenced by this p-d hybridization [4].

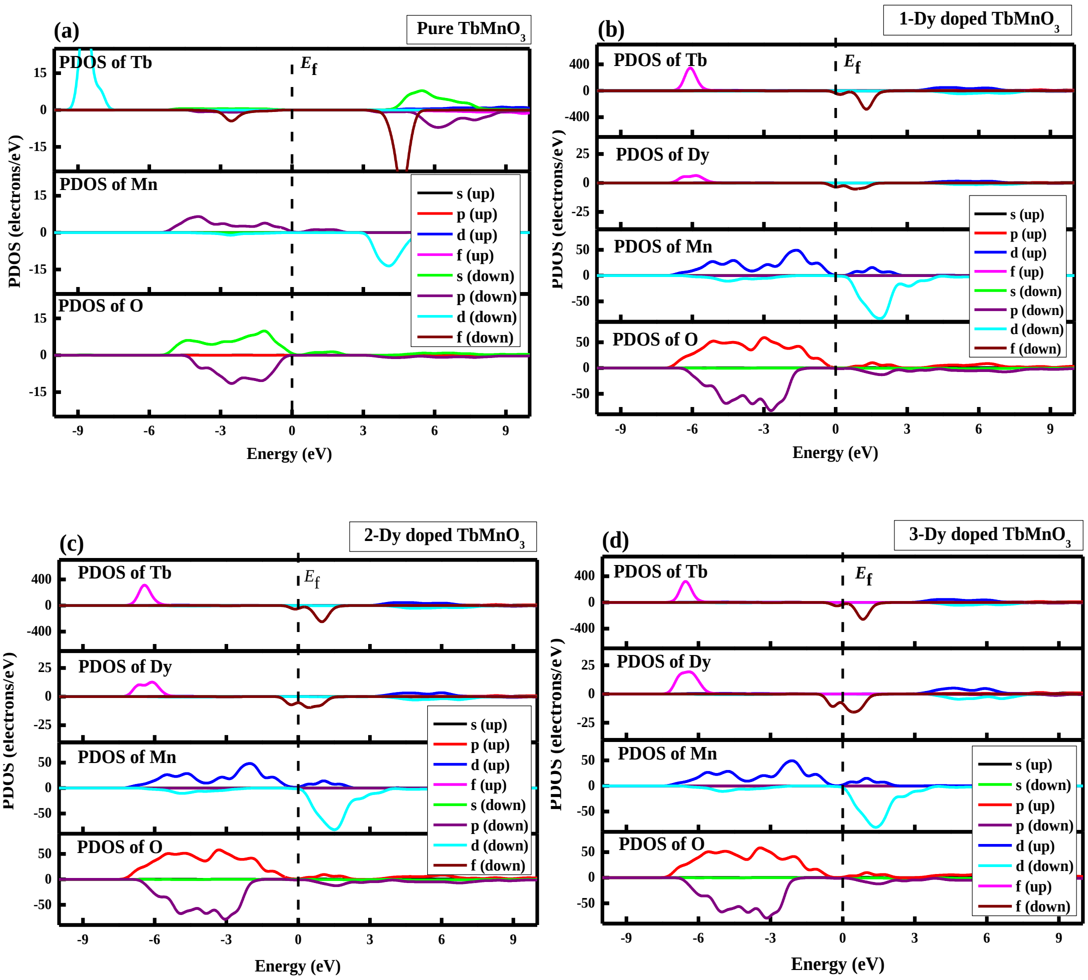

Figure 4.4: PDOS of **(a)** Pure $TbMnO_3$, **(b)** 1-Dy doped $TbMnO_3$, **(c)** 2-Dy doped $TbMnO_3$ and **(d)** 3-Dy doped $TbMnO_3$

The spin up VB mainly show contributions of 4f (spin up) states of Terbium along with 4f (spin up) states of Dysprosium, but the main contribution is from 3d (spin up) states of Manganese mixed with 2p (spin up) states of Oxygen while the spin down VB consists of O 2P (spin down) states. Meanwhile, Tb 5d (spin up) states combined with Dy 5d (spin up) states dominate the CB above the E_F, with energies ranging from 3.9 eV to 6.7 eV. The main contribution in spin down CB showed by Tb 4f (spin down) state mixed with Dy 4f (spin down) state.

Figure 4.3 shows the existence of DOS at E_F in the spin up and down channels, and Table 4.5 lists the calculated spin polarization (P_S). The calculated DOS at the E_F of pure TMO are 2.26 and 0.4 in spin-up and down channels respectively as presented in Figure 4.5 which produced spin polarization of 69.9 % and which is less than 80% which is required for spintronic RAM technology [25].

Table 4.5: Calculated DOS at EF in spin up g_n (E_F)↑ and spin down g_n (E_F)↓ channels with spin polarization (Ps) for pure and Dy doped TMO

Material	$g_n(E_F)_\uparrow$	$g_n(E_F)_\downarrow$	P_s
Pure	2.26	0.4	69.9%
1-Dy doped	6.57	44.2	74.3%
2-Dy doped	4.82	53.3	83.5%
3-Dy doped	3.06	41.6	86.3%

The spin polarization with different number of Dy atoms doped where the 1-Dy doped TMO shows spin polarization of 74.3 % at the Fermi level which is also less than 80 % in which 6.57 value is shared from $g_n(E_F)_\uparrow$ and 44.2 value is contributed by $g_n(E_F)_\downarrow$. Whereas Table 4.5 shows that spin polarization higher than 80% was obtained by 2-Dy and 3-Dy doped TMO in the orthorhombic phase. Thus, these systems are taken into consideration for more discussion. At the E_F, the 2-Dy doped TMO system showed 83.5% spin polarization, with the spin down channel contributing 53.3 and the spin up channel donating 4.82 values. The energy range of -2.5 to -6 eV in valence band is where the variation in the spin-down channel is observed. The 3-Dy doped TMO system has shown 86.3 % spin polarization at the E_F with the spin down channel contributing 41.6 and the spin up channel contributing 3.06.

4.3: Magnetic Properties

The total magnetic moment (M_{spin}) per unit Ω_o in units of μ_B of TMO system have been measured using equation 2.4 in which corresponding unit cell volume of pure and Dy doped TMO are taken from Table 4.2.

For pure TMO orthorhombic phase, a net magnetic moment of 10.65 μ_B has been observed with volume magnetization of 34.69 MA/cm which are comparable with previous reported values of magnetic moment [7][8]. Table 4.6 shows the calculated net magnetic moment, magnetic moment of each element Tb, O, Mn, and the volume magnetization for pure and Dy doped TMO in the orthorhombic phase. The individual magnetic moment ranges for Mn, O, and Tb in pure TMO are 4.24 to 4.25 μ_B, 0.10 to 0.26 μ_B, and 6.15 μ_B respectively.

Table 4.6: Magnetization and magnetic moments of pure and Dy doped TMO in orthorhombic phase

$TbMnO_3$ Material	Magnetic Moments (μ_B)				M (MA/cm)
	Tb	Mn	O	Total	
Pure	6.15	4.24	0.26	10.65	34.69
1-Dy doped	6.08	3.46	0.15	9.69	34.78
2-Dy doped	6.06	3.53	0.134	9.724	35.02
3-Dy doped	6.06	3.53	0.134	9.724	35.15

4.4: Bond Population Analysis

The information regarding the compound's bonding nature (metallic, ionic and covalent) acquired by Mulliken bond population analysis [73]. The change in the electronic structure with atomic displacement is quantified by the Mulliken charge, which is associated with the vibrational properties of compounds. It also has connections to polarizability, charge mobility in reactions, and other molecular system characteristics. The quantity of missing valence charges in a projection is referred to as the charge spilling parameter, and a compound with a small value suggests strong electronic bonding [74]. The atomic charges and spilling parameter calculated from these estimations are listed in Table 4.7. The charge spilling parameters for pure $TbMnO_3$ are 0.46% and 0.24% for spin up and down respectively which indicates presence of good electronic bonds. The present study indicates that Tb atom has a larger total charge than the Mn and O atoms which is due to the 4f state, although the other state as p contributes approximately half of the 4f state. Furthermore, it is noted that there are covalent bonds with an ionic contribution because the Mulliken value of the charges of the various atoms (Tb: +3, Mn: +2, and O: -2) differs from the formal charge predicted for a purely ionic state.

Table 4.7: Charge spilling parameter (%), atomic Mulliken charges, effective valence, and Hirshfeld charge of $TbMnO_3$

$TbMnO_3$ Structure	Charge spilling	Specie	Spin	Mulliken atomic Population					Mulliken Charge	Effective Valence	Hirshfeld Charge	Effective Valence
				s	p	d	f	Total				
Pure	0.46 (spin up) 0.27 (spin	Tb	up	1.15	3.32	0.72	7.00	12.19	0.73	6.10	0.32	4.24
			dn	1.16	3.27	0.64	1.01	6.08				
		Mn	up	1.00	3.00	4.75	0.0	8.75	1.86	4.36	0.70	6.15
			dn	1.00	3.00	0.39	0.0	4.39				
1-Dy doped	0.43 (spin up) 0.24 (spin down)	Tb	up	1.14	3.31	0.70	7.00	12.15	0.74	6.03	0.70	6.07
			dn	1.14	3.26	0.62	1.08	6.11				
		Dy	up	1.14	3.30	0.68	7.00	12.12	0.72	4.97	0.69	5.03
			dn	1.14	3.26	0.63	2.12	7.16				
		Mn	up	1.00	3.00	4.40	0.00	8.41	1.83	3.65	0.28	3.55
			dn	1.00	3.00	0.76	0.00	4.76				
2-Dy doped	0.43 (spin up) 0.24 (spin down)	Tb	up	1.14	3.30	0.70	7.00	12.15	0.74	6.04	0.71	6.08
			dn	1.14	3.26	0.62	1.08	6.11				
		Dy	up	1.14	3.30	0.69	7.00	12.12	0.73	4.95	0.69	5.03
			dn	1.15	3.27	0.63	2.12	7.17				
		Mn	up	1.00	3.00	4.41	0.00	8.41	1.84	3.66	0.30	3.72
			dn	1.00	3.00	0.75	0.00	4.75				
3-Dy doped	0.43 (spin up) 0.24 (spin down)	Tb	up	1.14	3.31	0.70	7.00	12.16	0.72	6.04	0.70	6.07
			dn	1.14	3.27	0.63	1.08	6.12				
		Dy	up	1.14	3.30	0.67	7.00	12.12	0.73	4.96	0.69	5.02
			dn	1.15	3.26	0.62	2.13	7.15				
		Mn	up	1.00	3.00	4.40	0.00	8.40	1.83	3.64	0.28	3.53
			dn	1.00	3.00	0.77	0.00	4.77				

An effective valence can also be used to determine the ionic or covalent nature of a chemical bond. An effective valence is the absolute numerical difference between the cation species' ionic charge and Mulliken charge [74]. An ideal ionic bond is signified by zero value of this factor, whereas increasing covalency is indicated by the values greater than zero. The calculated effective valence of all the cation species of pure and doped $TbMnO_3$ are presented in Table 4.7, which demonstrates that the Tb and Mn atoms in $TbMnO_3$ has higher effective valences which revealed the presence of both covalent and ionic character in the $TbMnO_3$. Electrons are transferred from Tb and Mn to O atoms according to Hirshfeld charge analysis.

Table 4.8 shows the bond length and bond population of pure and doped $TbMnO_3$. The shorter bond length, higher bond population and electron density exhibit increase in hardness and crystal stiffness. Bond populations overlap for pure $TbMnO_3$ exhibit a range of both negative and positive values. The positive (+) values represent interactions between atoms that are bonding, whereas negative (−) values signify interactions that are antibonding [75].

Table 4.8: Calculated Mulliken overlap population P^{μ}, and bond length d^{μ} (Å) of the pure and Dy doped $TbMnO_3$

$TbMnO_3$ Structure	**Bond**	**Population overlap (P^{μ})**	**Bond Length (d^{μ}) in Å**
Pure	Mn-O	-0.0033	2.009161
	Tb-O	0.2535	2.515333
1-Dy doped	Mn-O	0.0595	1.9052407
	Tb-O	0.3055	1.72782
	Dy-O	0.1096	2.429662
2-Dy doped	Mn-O	0.0462	1.09597
	Tb-O	0.2840	2.5485
	Dy-O	0.3415	2.48185
3-Dy doped	Mn-O	0.04	2.058
	Tb-O	0.32	2.48145
	Dy-O	0.321	2.487

From Table 4.8, it is observed that Mn–O shows anti-bonding character in most $TbMnO_3$. While the Tb–O and Dy-O exhibit bonding nature. Thus, the values of bond overlap population for pure $TbMnO_3$ suggests the existence of both anti-bonding and bonding-type interactions. Table 4.8 shows the existence of both covalent and ionic bonding for pure and Dy doped $TbMnO_3$.

4.5: Optical properties

The optical properties including refractive index, dielectric function, conductivity, loss function, absorption, and reflectivity of pure and Dy doped TMO in orthorhombic phase have been calculated with DFT analysis to explore the behavior of monoatomic, diatomic, and triatomic substitution of Dy atoms in TMO for low energy switching spintronic technology.

4.5.1: Dielectric function

The energy-dependent optical properties can studied the state of impurity levels, specific magnetic excitations, localized defects, excitons, energy band structure, and lattice vibrations [76]. The calculations of electronic band structure are used to get the dielectric function, which is a crucial factor in understanding optical properties. The complex dielectric function varying with energy can predict how a material's linear response to an external electromagnetic field.

At equilibrium lattice constants, the dielectric functions of $TbMnO_3$ have been calculated based on electronic structure, for the frequency range up to 8 eV. The dielectric constant is calculated by equation 3.1. All values of dielectric constants have been calculated at nearly 0 frequency from dielectric graphs of pure and Dy doped $TbMnO_3$ as shown in Figure 4.7 where $\varepsilon_1(\omega)$ is representing the real part and $\varepsilon_2(\omega)$ is representing the imaginary parts. The group velocity of the incident electromagnetic wave in the material and the energy absorption from the incident electromagnetic field within the material because of dipole motion are represented by the imaginary and real components of the dielectric function. Intra-band transitions are fundamental at low energies whereas the inter-band term is highly dependent on the specifics of the electronic band structure [76].

The permittivity component is the real part of the dielectric function which is directly proportional to the field amplitude and measures the stored energy. Higher dielectric constants are desirable for better applications of optoelectronic devices. At zero-frequency limit, the static dielectric constant is written as $\varepsilon_1(0)$ which demonstrates the material's response to a static electric field [74]. The calculated dielectric function (ε_1) of pure TMO is 6.14.

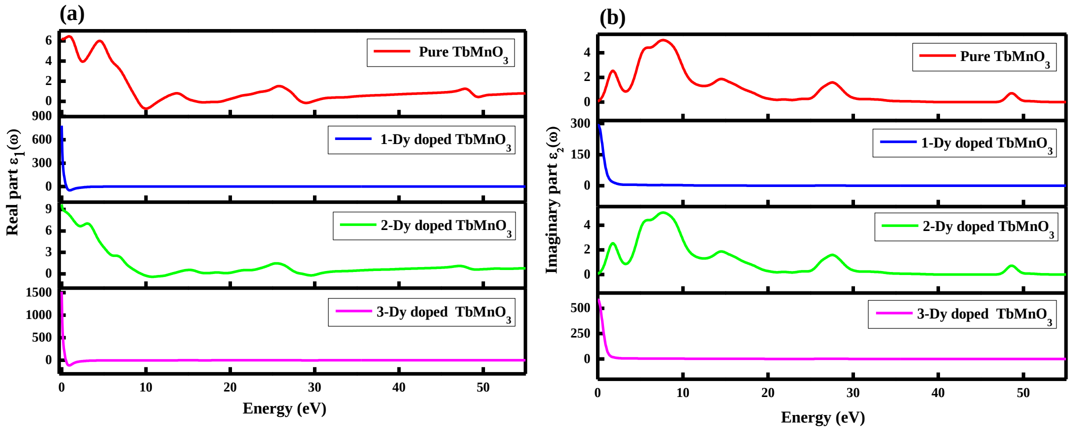

Figure 4.5: Dielectric functions of pure and doped $TbMnO_3$ **(a)** real part of dielectric function **(b)** imaginary part of dielectric function

Figure 4.5 (a) shows $\varepsilon_1(\omega)$ decreases with increase in frequency $\varepsilon_1(\omega)$ in which four various types of polarization are contributed mainly such as dipolar, atomic, interfacial and electronic polarization. At low frequency $\varepsilon_1(\omega)$ shows high value by the contributions of all polarizations. While the interfacial part becomes insignificant at higher frequency. Due to inertia of atoms and ions, dipolar and atomic contributions diminish with further increase in frequency and only electronic contribution is present which results reduction in $\varepsilon_1(\omega)$ [8].

The dielectric function $\varepsilon_2(\omega)$ is directly linked to the transitions from occupied to unoccupied states. The several obvious peaks shown by absorptive part of dielectric function signify the electronic transition from occupied to unoccupied states. The second peak is higher and very prominent than the other peaks, and it is primarily corresponding to the transitions between the Mn 3d states and conduction bands, or the occupied O 2p to unoccupied Mn 3d states or the d–d transition. The other peaks are visible at the transitions from the O 2p VB to the higher-energy CBs of Mn 3d or Tb 4f. The transition of inner electrons from O 2s level to the CB is thought to be responsible for the last peak. It should be noted that the band structure might include direct or indirect transitions with energy corresponding to the same peak, so the peak in ε_2 does not necessarily indicate the inter-band transition [44]. The variation in the dielectric functions is given in Table 4.9.

Table 4.9: The calculated values of dielectric functions for pure and doped TMO

$TbMnO_3$ material	Dielectric function $\varepsilon_1(\omega)$	Dielectric function $\varepsilon_2(\omega)$
Pure	6.14	4.98
1-Dy doped	782.90	282.70
2-Dy doped	9.67	5.50
3-Dy doped	1520.65	573.38

The calculated static dielectric constant ε(0) of pure TMO in orthorhombic phase using equation 3.1 is found 6.14 which is consistent with reported theoretical data (5.85) and shows the semiconductor nature of TMO in orthorhombic phase [44] which increases with the substitution of Dy element. Both imaginary and real parts of dielectric function change their values with the increasing concentration of dopant (Dy).

4.5.2: Refractive index

The material's refractive index is important for the development of optimal electrical devices. The refractive index is used to calculate the electromagnetic wave's phase velocity in a medium, while the attenuation is determined by the imaginary part when an electromagnetic wave traverses a material.

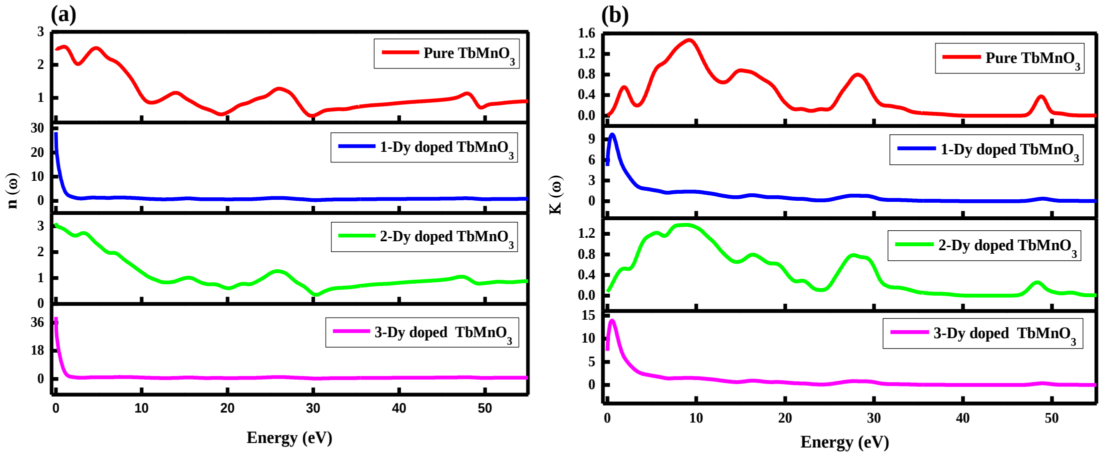

Figure. 4.6: calculated n and k of pure and doped $TbMnO_3$ **(a)** refractive index (n) and **(b)** extinction coefficient (k)

The n(ω) is calculated using equation 3.2 and extinction constant using equation 3.3. The static refractive index n (0) is observed 2.50 for pure $TbMnO_3$. The maximum peak of pure $TbMnO_3$ shows a refractive index (n) with a value of 2.6 at 1.04 eV while the second peak has value around 2.50 at 4.75 eV and then with the increase in incident energy to 10.32 eV its value drops to almost 0.87 as shown in Figure 4.6 (a). Then, there is a little increase in the refractive index and after 50 eV it remains nearly constant. Simultaneously, the minima of extinction coefficient k (ω) also calculated as shown in Figure 4.6 (b). The maximum peak of extinction constant has value of 1.44 at 8.87 eV. It decreases to almost zero and becomes nearly constant after 53 eV.

Table 4.10: Refractive index (n) for Pure and doped $TbMnO_3$

$TbMnO_3$ Structure	**1st Peak**	**Energy (eV)**	**2nd Peak**	**Energy (eV)**
Pure	2.50	0.01	2.50	4.75
1-Dy doped	28.1	0.01	---	---
2-Dy doped	3.07	0.01	2.73	3.20
3-Dy doped	39.57	0.01	---	---

The static refractive index n (0) for monoatomic, diatomic, and triatomic substitution of Dy element is about 28.1 (at 0.01 eV), 3.07 (at 0.01 eV) and 39.57 (at 0.01 eV) respectively. The values of the first two peaks of refractive index (n) for pure and doped $TbMnO_3$ are given in Table 4.10. The values of refractive index (n) for first peak increases for monoatomic substitution and then decreases in diatomic substitution but with the substitution of triatomic Dy element the first peak's value of refractive index again increases. The relation between $\varepsilon_1(0)$ and n(0) as well as the inverse relation between band gap and refractive index are confirmed by their values [77].

4.5.3: Absorption

The absorption coefficient measures how much degradation of light intensity occurs in a medium per unit length traveled. The absorption vs frequency graph in Figure 4.7 shows that spectra do not initiate at zero energy and exhibit a gradual rise as photon energy increases, providing further evidence of its semiconducting nature. The maximum absorption is observed in the ultraviolet (UV) region for both pure and doped $TbMnO_3$ which correspond to their large band gap values. The various peaks of absorption consistent with the $\varepsilon_2(\omega)$ because of the different transitions of inter band [74]. The linear absorption spectrum exhibits three variations before reaching a highest value at 28.3 eV and declines to zero at approximately 40 eV. Meanwhile, absorption spectrum has a wider range between 0 eV to 40 eV than the width between 46 eV and 53 eV. The absorption is calculated by equation 3.6.

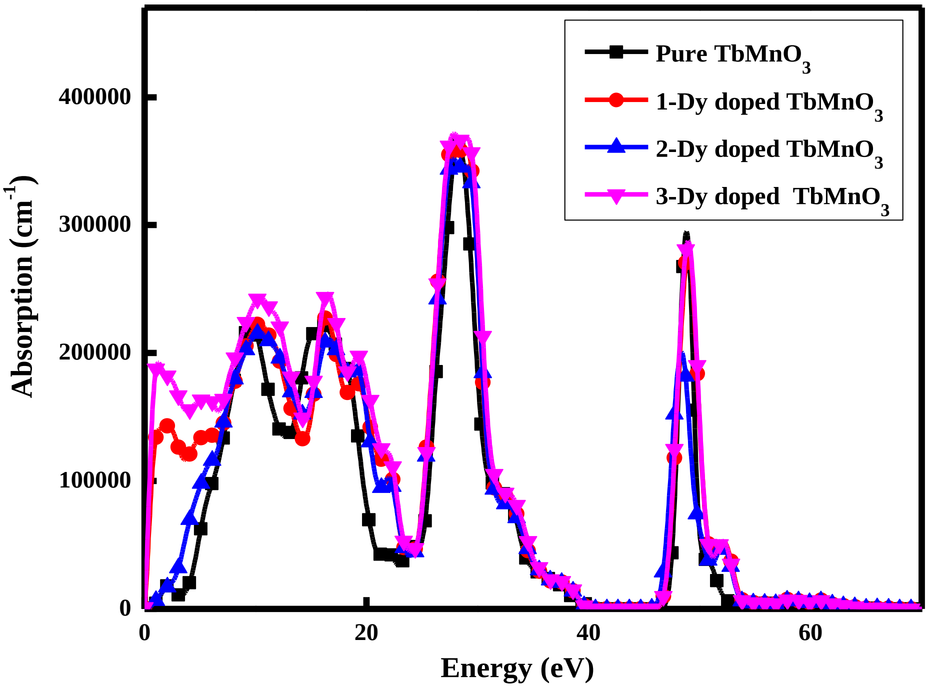

Figure 4.7: Absorption vs frequency of pure and doped TbMnO$_3$

The reflectivity is minimum in the 0 to 23 eV energy range and three minima observed at about 2 eV, 9.7 eV and 16 eV which correspond to the three anomalies in absorption spectra. Absorption peaks change with the substitution of Dy atoms as given in Table 4.11. The maximum peaks of monoatomic, diatomic, and triatomic substitution of Dy are about 363320.79 (at 27.7 eV), 350708.70 (at 27.87 eV) and 370451.25 (at 28.09 eV) respectively and then sharply declines to zero at 40 eV. Similarly, the pure TbMnO$_3$ has a wider absorption spectrum between 0 eV to 40 eV than the absorption between 46 eV to 53 eV.

Table 4.11: Absorption peaks of Pure and doped TbMnO$_3$

TbMnO$_3$ Structure	**Maximum Peaks**	**Energy (eV)**
Pure	362837.352	28.30
1-Dy doped	363805.448	27.7
2-Dy doped	351650.343	27.87
3-Dy doped	370160.621	28 .09

4.5.4: Reflectivity

The reflectivity vs frequency graph is shown in Figure 4.8. Reflectivity is calculated using equation 3.4. A lower energy band gap in terms of reflectivity results in a higher $\varepsilon_1(0)$ value which in turn leads to a higher R(ω) and vice-versa.

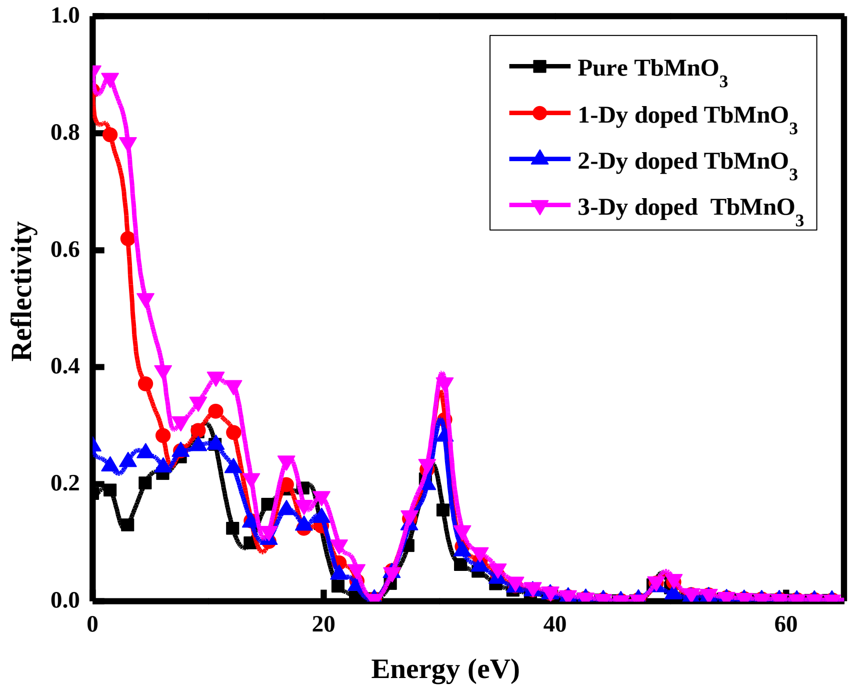

Figure 4.8: Reflectivity vs Frequency for pure and doped $TbMnO_3$

The reflectivity which is calculated reached to the highest value of 0.30 nearby 9.82 eV then decreases to zero at 23.4 eV. The reflectivity changes with the increase in number of dopants (Dy). For 1, 2 and 3 Dy doped TMO structure the maximum peaks shift to 0.81 (at 1.04 eV), 0.31 (at 30 eV) and 0.89 (at 1.32 eV) respectively. The variation in the peaks of reflectivity for pure and doped $TbMnO_3$ are given in Table 4.12.

Table 4.12: Reflectivity peaks of Pure and doped TMO

$TbMnO_3$ material	**Maximum Peaks**	**Energy (eV)**
Pure	0.304	9.81
1-Dy doped	0.814	1.22
2-Dy doped	0.312	30.10
3-Dy doped	0.889	1.32

4.5.5: Conductivity

The key optical parameter to understand the electromagnetic response is optical conductivity. The conductivity displayed by free charge carriers within a particular photon energy range defines the material's photo-conductivity is defined by the conductivity It is exhibited by free charge carriers within a specific range of photon energy characterizes [74]. The plotted conductivities are shown in Figure 4.9 (a & b). The pure $TbMnO_3$ has the highest peak, with a value of 5.28 at 27.69 eV for real.

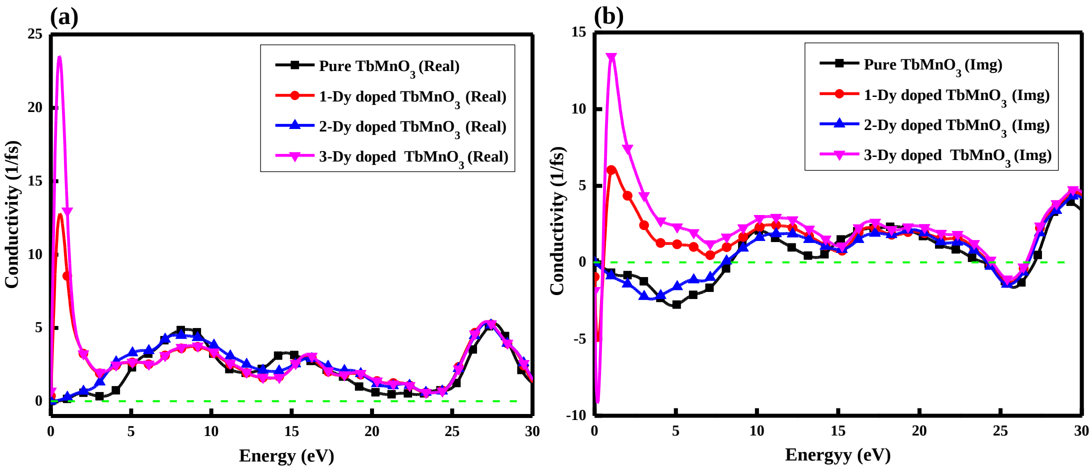

Figure 4.9: Conductivity of Pure and doped $TbMnO_3$ (a) real Part (b) Imaginary part

With the substitution of one Dy atom the highest peak of conductivity shifted to 12.74 at 0.61 for real. For substitution of two Dy atoms the value of highest peak is 5.34 at 27.16 eV for real. The highest peak for substitution of three Dy atoms has value of 23.48 at 0.56 eV for real. The variation in the real and imaginary part of conductivity is shown in Table 4.13. The highest peak of imaginary part of conductivity is 4.02 at 29.11 eV which changes to 6.12 at 1.22 eV, 4.30 at 29.85 and 13.49 at 1.07 with doping of 1, 2 and 3-Dy atoms doping respectively.

Table 4.13: Conductivity peaks of Pure and doped TMO

$TbMnO_3$ material	**Real part**	**Energy (eV)**	**Imaginary Part**	**Energy (eV)**
Pure	5.28	27.69	4.02	29.11
1-Dy doped	12.72	0.61	6.12	1.22
2-Dy doped	5.32	27.16	4.30	29.85
3-Dy doped	23.48	0.56	13.49	1.07

4.5.6: Loss Function

The loss function depicts that when a fast electron passes through a substance how much energy loses which is determined by its reflection and absorption properties. [74]. Fig. 4.10 shows spectra of energy-loss which explain the loss of energy in the pure and doped TMO. The frequency of bulk plasma ω_p occurs when $\varepsilon_2 < 1$ and ε_1 reach the zero point generally defined the main peaks in loss function. [44].

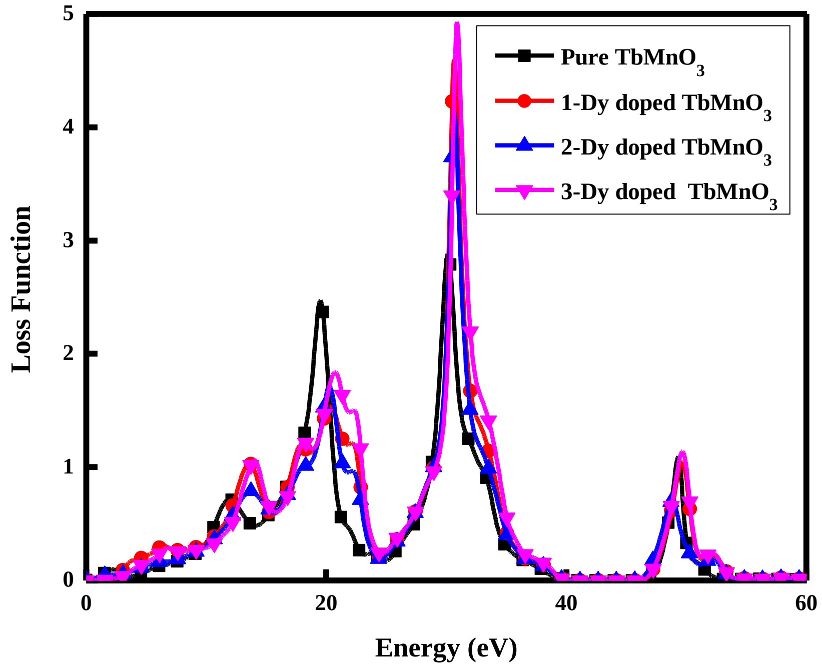

Figure 4.10: Loss Function of Pure and doped $TbMnO_3$

The sudden decrease in reflectivity corresponds to a major peak in loss spectrum at 30 eV for $TbMnO_3$. This process is associated to the transition between the filled O 2s bands and the empty conduction band [44]. Loss function is calculated by equation 3.5. The loss function changes with the increasing number of Dy atoms is given in Table 4.14. The main peaks for monoatomic, diatomic, and triatomic substitution of Dy element are 4.62 (at 30 eV), 4.11 (at 30 eV) and 4.91 (at 30 eV) respectively.

Table 4.14: Loss Function peaks of Pure and doped TMO

$TbMnO_3$ material	**Maximum Peaks**	**Energy (eV)**
Pure	2.88	30.1
1-Dy doped	4.59	30.68
2-Dy doped	4.13	30.66
3-Dy doped	4.90	30.93

CHAPTER 5

DISCUSSION

5.1 Introduction

This chapter examines the trend and presents the findings for the pure and Dy-doped $TbMnO_3$ (TMO) by theoretical treatment. The trend between all the values (like equilibrium lattice constants, density of state (DOS), volume of optimized cell, spin polarization, magnetization, band structures, optical properties, partial density of state (PDOS) and dielectric constant) with the increasing number of Dy-doped $TbMnO_3$ super cells for orthorhombic phase are presented and discussed.

5.2 Crystal Structure

The graph between optimized lattice constants and number of Dy dopant atoms is shown in Figure 5.1. This variations in lattice constant are due to smaller ionic radius of Dy^{3+} (108.3 pm in 9-coordination) than Tb^{3+} (109.5 pm in 9-coordination) [50, 51, 61]. The lattice constant “a & b” are overall decreased as compared to the lattice constants of pure TMO while the lattice parameter “c” is increased.

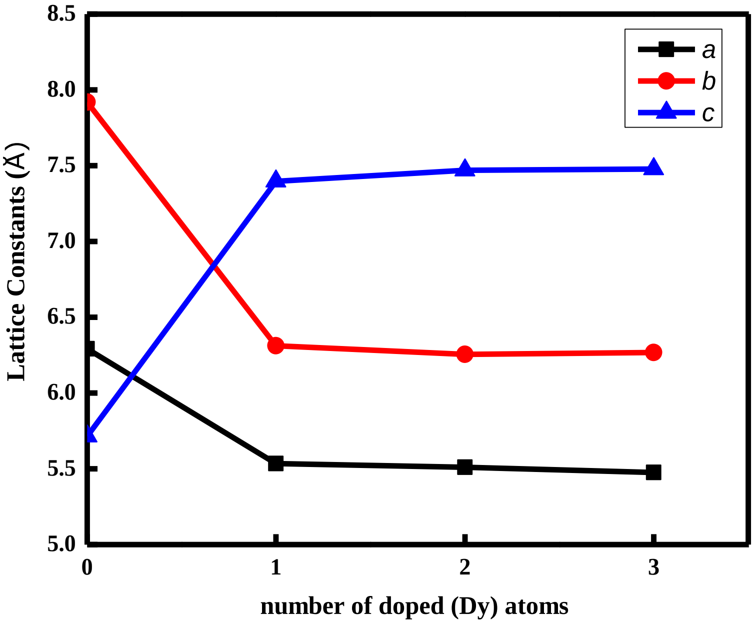

Figure 5.1: Variation of lattice parameters a, b and c with increasing number of Dy atoms for pure and doped TMO

Figure 5.2 (a-b) shows the variation in the bond lengths and bond angles with addition of Dy atoms. The Mn-O-Mn bond angles are increased as compared to pure TMO while the Mn-O bond lengths are decreased in general then pure TMO. The Mn-O-Mn bond angles increased due to the difference in ionic radius of dopant (Dy) and Tb [61, 63, 65] up to substitution of two Dy atoms. However, upon substitution of third Dy atom, the Mn-O-Mn bond angles decreased as shown in Figure 4.3. The bond angles and bond lengths are changed with increase in number of Dy atoms due to lattice distortion.

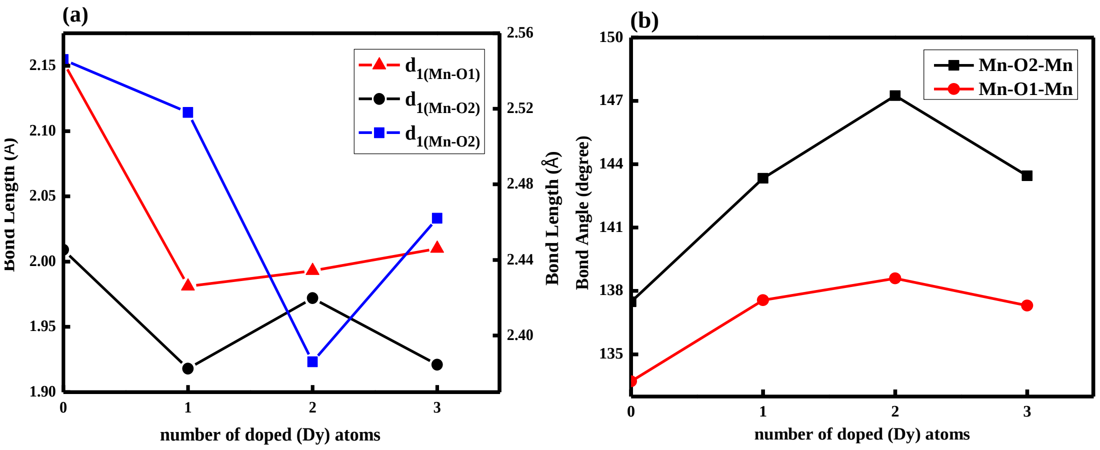

Figure 5.2: Trend graph of Pure and Dy doped $TbMnO_3$ (a) Bond lengths (b) Bond angles

5.3: Band Structure and Density of States (DOS)

Figure 5.3 (a) shows the changes in the band structures with addition of Dy atoms in pure TMO while the Figure 5.3 (b) shows the contribution of dopant (Dy) orbitals near Fermi level.

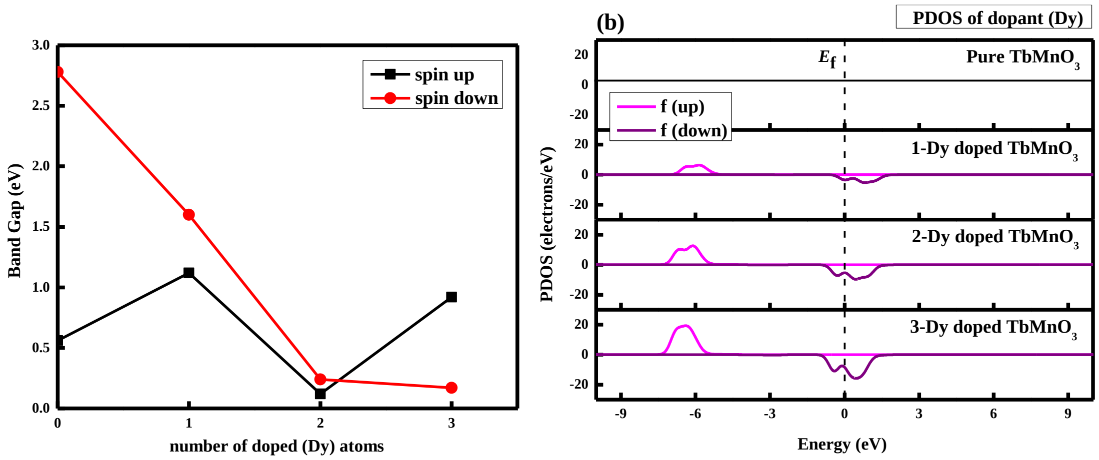

Figure 5.3: Trend graph between numbers of doped atoms vs (a) Band gap (b) PDOS of dopant (Dy)

The band gap variation occurs due to the distortion in the lattice parameters and Dy atom introduces additional electronic states in the vicinity of its location in the super cell [8, 47, 50, 51, 65, 70]. This lead to localized changes in the electronic structure, affecting the band gap near the doping site. Figure 5.3 (b) shows that as the number of

Dy atoms increase its contribution increase across the Fermi level due to 4f orbital in both states (spin up and spin down).

5.4 Spin Polarization and Volume Magnetization

Figure 5.4 (a) shows the changes of Spin polarization vs number of doped (Dy) atoms. Spin polarization is increased overall as compared to pure TMO. Dysprosium is a rare-earth element known for its strong magnetic moments. When Dy is added to a pure TMO, it interacts with the local magnetic moments of the transition metal ions in the TMO lattice, influencing the overall magnetic behavior of the material. Dysprosium itself has a high magnetic moment (5.03 μ_B) due to its partially filled f-electron shell (as shown in Figure 5.3-b). When incorporated into a TMO, its magnetic moments can contribute to the overall magnetization of the material [7], influencing spin polarization. The addition of dysprosium may also modify the electronic structure of the TMO. Changes in the DOS or value of band gap near E_F [46] can affect the magnetic properties and spin polarization.

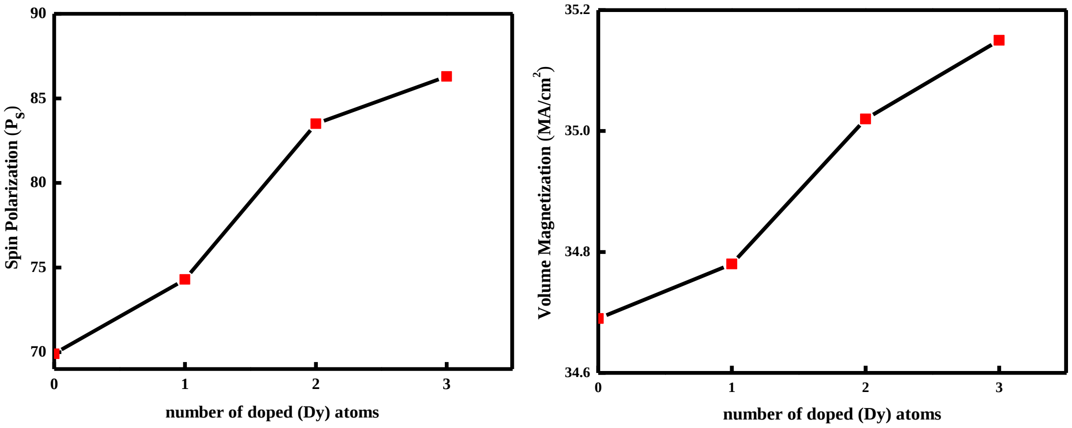

Figure 5.4: Trend graphs of Pure and doped TMO between numbers of doped atoms vs **(a)** Spin Polarization **(b)** Volume Magnetization

Figure 5.4 (b) shows the changes of volume magnetization with numbers of Dy atoms. There is an overall increase in magnetization as compared to pure TMO. Spin polarization is proportional to Volume magnetization. The material's magnetic properties are majorly effected by exchange interactions between magnetic ions. Dysprosium, being a rare earth element with a strong magnetic moment, can introduce additional exchange interactions in the system. This can enhance the alignment of magnetic moments, leading to an increase in volume magnetization [51, 61].

5.5 Bond Population Analysis

Figure 5.5 (a-b) shows the population overlap and bond length of Tb-O, Mn-O and Dy-O with the increase numbers of Dy atoms. The change in bond population overlap and bond length in a material $TbMnO_3$ with the addition of Dy which can be influenced by various factors, including electronic structure modifications, crystal structure changes, and the interaction between different elements. The substitution of Dy with Tb in the crystal lattice of $TbMnO_3$ may lead to changes in bond lengths due to ionic radii difference of Tb and Dy. Dy is smaller than Tb, and this substitution can cause distortion in the crystal structure which leads to longer bond angles. The introduction of Dy may induce variations in the electronic structure of the TMO material. Dy has a different electron configuration compared to Tb, and this can affect the bonding between atoms. Changes in the electronic structure can influence the bond population overlap, leading to variations in bond lengths. The substitution of Dy with Tb may induce charge transfer effects or alter the polarization of the material. This can influence the distribution of electron density around atoms, affecting bond lengths and bond population overlap. Magnetic interactions between the magnetic moments are associated with Tb, Mn, and Dy ions which can influence the crystal structure.

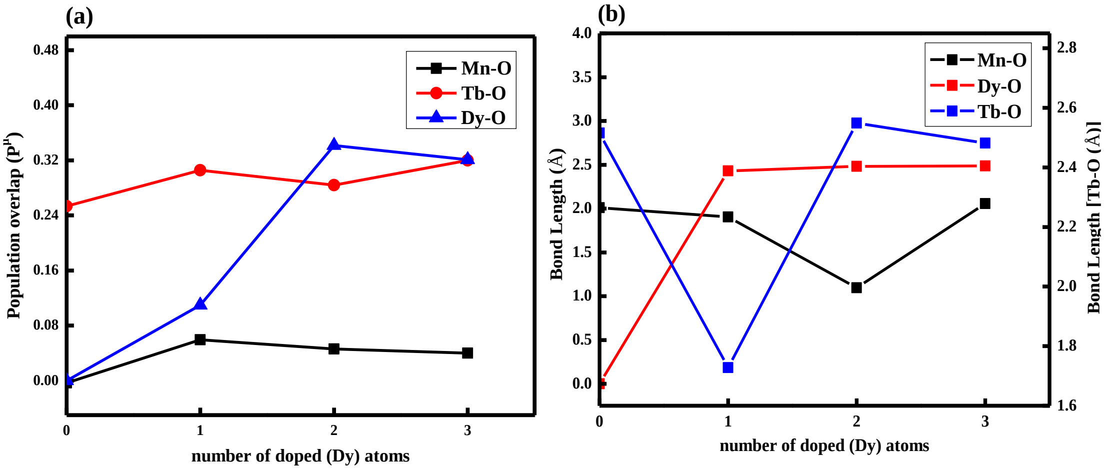

Figure 5.5: Variation of Pure and Dy doped $TbMnO_3$ (a) Population overlap vs number of Doped atoms (b) Bond length vs number of Dy doped atoms

Changes in the magnetic ordering and spin configurations can affect the bond lengths [7, 51, 61] and overlap by modifying the electron distribution within the material. The addition of Dy may induce lattice distortions [50, 51, 61] or alter the symmetry of the crystal structure. These distortions can affect the bond lengths and the degree of overlap between atomic orbitals.

5.6 Dielectric constant and Optical Properties

Figure 5.6 shows the variation in the imaginary and real parts of dielectric function for pure and Dy doped $TbMnO_3$ with the addition of Dy atoms. There is an increase in the dielectric functions overall with addition of Dy-dopant atoms in TMO structure. Dielectric functions increase with the substitution of one Dy atom and decrease again with the substitution of two Dy atoms. While with the doping of three Dy atoms, dielectric functions again increase as shown in Figure 4.8. The Dy atom may induce local lattice distortions due to differences in size and charge between to Tb and Mn. These distortions can affect the dielectric function by influencing the phonon modes and electronic transitions in the material. The Dy 4f orbitals may hybridize with the surrounding O 2p and Mn 3d orbitals, leading to changes in the electronic structure and influencing the dielectric function [9].

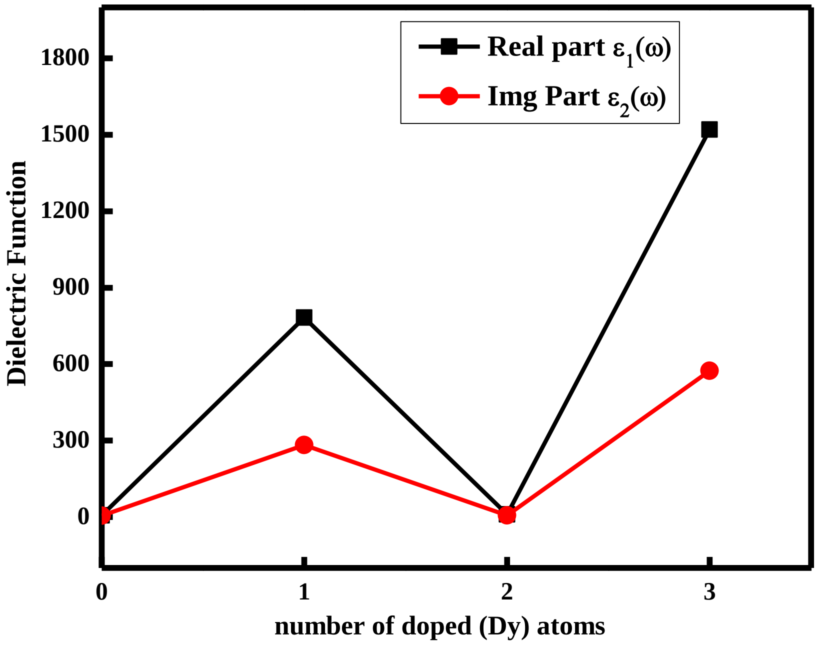

Figure. 5.6: Variation in dielectric functions of pure and doped $TbMnO_3$ real part (ε_1) and imaginary part (ε_2)

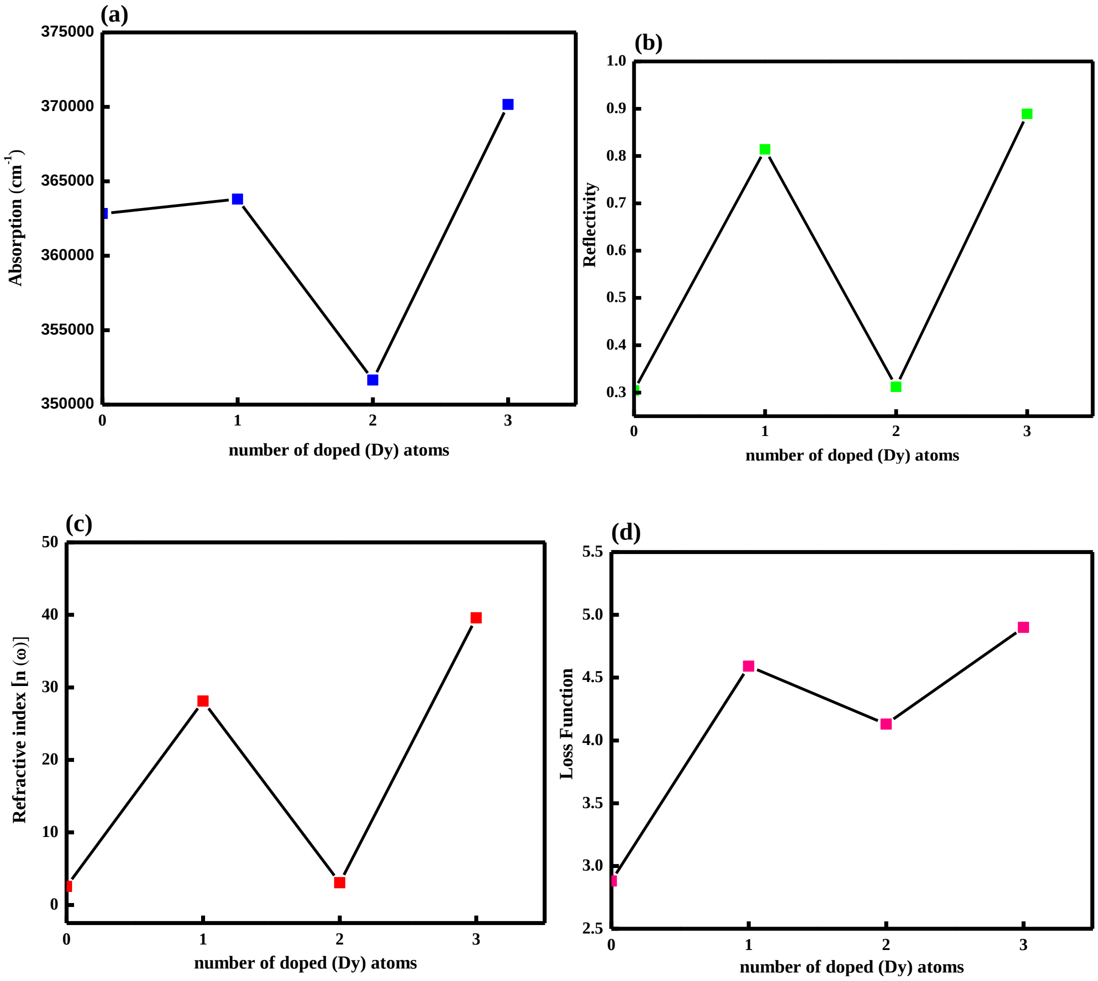

Figure 5.7: Variation of Optical properties vs number of Dy doped atoms for Pure and doped TbMnO$_3$ (a) Absorption (b) Reflectivity (c) Refractive index (d) Loss Function

Figure 5.7 (a-d) shows the variation in the optical properties with the addition of Dy atoms, there is an increase in each value as compared to Pure TMO. First the refractive index increases with addition of 1-Dy atom and then decreases with the addition of two Dy atoms and again increases with addition of 3-Dy atoms. Figure 5.6 (a-d) shows the same trend for all optical properties.

Doping introduces additional electronic states into the material due to the size difference of Dy and Tb, altering its electronic structure, affecting the positions and intensities of electronic states. Changes in the electronic structure [44, 64, 69, 76] can lead to shifts in the values of refractive index, reflectivity, absorption and Loss Function.

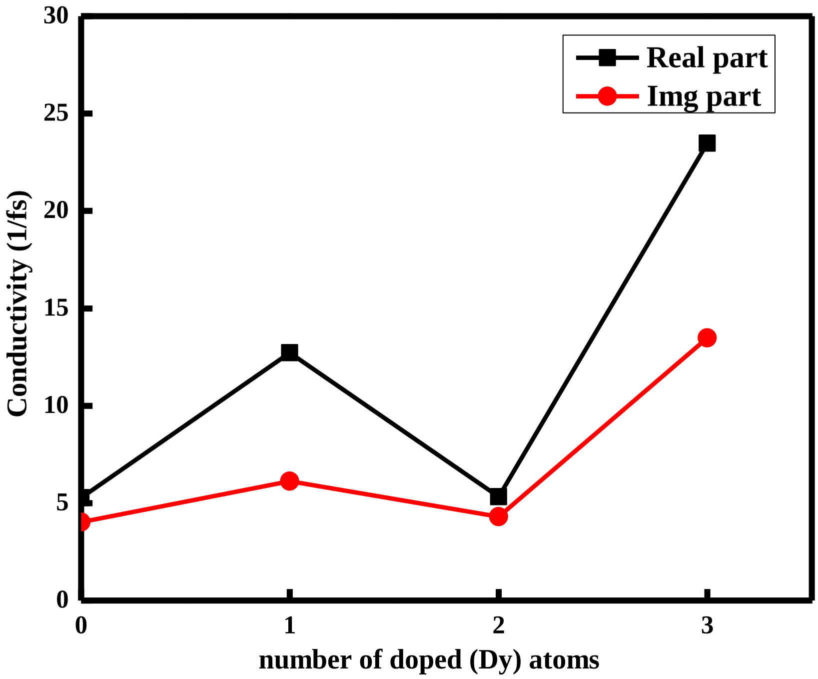

Figure 5.8: Variation of Conductivity vs number of doped (Dy) atoms for Pure and doped $TbMnO_3$

Figure 5.8 shows the variation in conductivity with the increased number of Dy dopant atoms. Overall, there is an increase in real and imaginary part of conductivity as compared to pure TMO. Doping with Dy can introduce additional charge carriers into the crystal lattice. The electronic configuration of Dy may contribute extra electrons or holes to the system, leading to changes in the overall charge carrier concentration. This alteration in the carrier density can influence the electrical conductivity. Both Tb and Dy are magnetic elements, and their interaction with the magnetic moments in $TbMnO_3$ can influence the electronic properties [8, 47, 50, 51, 65, 70]. Changes in the magnetic ordering or spin configuration can impact the electronic transport properties, leading to variations in conductivity.

CHAPTER 6

CONCLUSION

6.1: Conclusion

By employing first principles computations using GGA function in CASTEP numerical coding, the electrical and optoelectronic characteristics of pure and Dy-doped $TbMnO_3$ orthorhombic structure have performed successfully.

The calculated structural parameters agreed well with the reported data. The lattice parameters change with the substitution of 1, 2 and 3-Dy atoms with Tb in TMO 2×2×2 super cell. The "a, and b" lattice parameters decrease while the "c" lattice parameter increases with the addition of Dy atoms. The Mn-O-Mn bond length is also increased with the addition of Dy atoms.

The band structure of pure $TbMnO_3$ shows a direct band gap of 2.78 eV and 0.56 eV for spin down and up channel respectively. For 3-Dy doped $TbMnO_3$, the spin up band gap value increases to 0.92 eV while the spin down band gap value decreases to 0.17 eV. According to the DOS data, the considerable hybridization between O-2p and Mn-3d states is mainly responsible for the lower conduction band and upper valence band. Bond analysis and Mulliken charge is supported by the distribution of charge density which helps to predict the nature of bonding and anti-bonding. The bond population overlap between Mn-O, Tb-O and Dy-O is increased with the increase in number of Dy atoms.

The spin polarization of pure $TbMnO_3$ is obtained 69.9 % which increases to 86.3 % with introduction of 3-Dy atoms which is suitable for spintronic memory devices (>80 %). The volume magnetization for pure TMO is 34.69 MA/cm and increases to 35.15 MA/cm with introduction of 3-Dy atoms which shows the highest magnetization as compare of 1-Dy and 2-Dy doped TMO.

The optical properties for pure and Dy doped $TbMnO_3$ have also been evaluated which includes dielectric constants, refractive index, conductivity, loss function, absorption, reflectivity, and extinction coefficient. The dielectric constant of pure TMO is observed 6.14 which increased to 1520.65 with the introduction of 3-Dy atoms.

Optical behavior confirms the semiconducting nature of $TbMnO_3$. It is also found that in the low energy regions orthorhombic structures show significant optical anisotropy.

Furthermore, optical analysis suggests that the $TbMnO_3$ is a promising option for applications of UV-based optical device due to its optical anisotropy.

6.2: Future outlook

The magnetization observed from 1-Dy, 2-Dy and 3-Dy doped TMO is still a weak magnetization as compared to the value 500 MA/cm which cannot store much data. One major problem that persists with TMO is its weak magnetization per unit volume. Future research will examine orthorhombic phase TMO with all possible minimal doping concentration impurities like bismuth and aluminum at Tb-site and metals (X= Fe, Co) at Mn-site for 2×2×2 supercell to manipulate the magnetic and dielectric properties of TMO. Further Spin polarized geometry optimization will be performed for doped $TbMnO_3$ structures.

References:

[1] Hirohata, A.,Yamada, K.,Nakatani, Y.,Prejbeanu, L.,Diény, B.,Pirro, P.,Hillebrands, B. (2020). "Review on spintronics: Principles and device applications", *Journal of Magnetism and Magnetic Materials*, Vol. 509, pp. 166711. doi:10.1016/j.jmmm.2020.166711

[2] Yakout, S. M. (2021). "Spintronics and innovative memory devices: a review on advances in magnetoelectric BiFeO3", *Journal of Superconductivity and Novel Magnetism*, Vol. 34, no. 2, pp. 317–338. doi:10.1007/s10948-020-05764-z/Published

[3] Ali, S. E. (2022). "Influence of preparation method on phase formation, structural and magnetic properties of BiFeO3", *Journal of Electroceramics*, Vol. 48, no. 2, pp. 95–101. doi:10.1007/s10832-021-00276-1

[4] Kassimi, F. Z.,Zaari, H.,Benyoussef, A.,Rachadi, A.,Balli, M.,El Kenz, A. (2022). "A theoretical study of the electronic, magnetic and magnetocaloric properties of the TbMnO3 multiferroic", *Journal of Magnetism and Magnetic Materials*, Vol. 543, pp. 168397. doi:10.1016/j.jmmm.2021.168397

[5] Kassimi, F. Z.,Zaari, H.,Benyoussef, A.,Rachadi, A.,El Kenz, A. (2022). "Electronic, Magnetic, Electric and Magnetocaloric Properties of the Multiferroic Orthorhombic YMnO3", *Journal of Superconductivity and Novel Magnetism*, Vol. 35, no. 9, pp. 2493–2503. doi:10.1007/s10948-022-06217-5

[6] Selmani, Y.,Mouatassime, M.,Goumrhar, F.,Labrim, H.,Bahmad, L.,Benyoussef, A. (2021). "Structural, electronic and magnetic properties of the perovskite Ymno3", *Solid State Communications*, Vol. 328, pp. 114254. doi:10.1016/j.ssc.2021.114254

[7] Pérez, F.,Heiras, J.,Escudero, R. (2007). "Magnetic properties of multiferroic TbMnO3 doped with Al", *Physica Status Solidi (C) Current Topics in Solid State Physics*, Vol. 4, no. 11, pp. 4049–4053. doi:10.1002/pssc.200675901

[8] Das, A.,De, S.,Bandyopadhyay, S.,Chatterjee, S.,Das, D. (2019). "Modified dielectric and magnetic properties of Fe and Co substituted TbMnO3 nanoparticles", *Journal of Alloys and Compounds*, Vol. 778, pp. 839–847. doi:10.1016/j.jallcom.2018.11.170

[9] Xu, J.,Cui, Y.,Xu, H. (2014). "Improvements of dielectric properties of Fe doped TbMnO3", *Ceramics International*, Vol. 40, no. 8, pp. 12193–12198. doi:10.1016/j.ceramint.2014.04.060

[10] Xu, J.,Cui, Y.,Xu, H. (2016). "Dielectric properties of TbMnO3 ceramics doped with Bi and Fe ions", *Results in Physics*, Vol. 6, pp. 811–816. doi:10.1016/j.rinp.2016.10.018

[11] Zhang, C.,Yan, H.,Wang, X.,Kang, D.,Li, L.,Lu, X.,Zhu, J. (2013). "Effect of A-site Bi-doping on the magnetic and electrical properties in TbMnO3", *Materials Letters*, Vol. 111, pp. 147–149. doi:10.1016/j.matlet.2013.08.068

[12] Guo, Y. Y.,Guo, Y. J.,Zhang, N.,Lin, L.,Liu, J. M. (2012). "Suppression of ferroelectricity and quantum fluctuations in Ru-doped TbMnO 3", *Applied Physics A: Materials Science and Processing*, Vol. 106, no. 1, pp. 113–117. doi:10.1007/s00339-011-6575-x

[13] Kumar, N. P.,Sagar, E.,Babu, P. D.,Srinivas, A.,Raja, M. M. (2019). "Investigation of low temperature magnetization, specific heat and magnetocaloric effect in Ho doped TbMnO3 multiferroic system", *Solid State Sciences*, Vol. 94, pp. 54–63. doi:10.1016/j.solidstatesciences.2019.05.017

[14] Cui, Y. (2008). "Decrease of loss in dielectric properties of TbMnO3 by adding TiO2", *Physica B: Condensed Matter*, Vol. 403, no. 18, pp. 2963–2966. doi:10.1016/j.physb.2008.02.036

[15] Manipatruni, S.,Nikonov, D. E.,Liu, H.,Young, I. A. (2015). "Spin-Orbit Logic with Magnetoelectric Nodes: A Scalable Charge Mediated Nonvolatile Spintronic Logic". doi:10.48550/arXiv.1512.05428

[16] Hu, J. M.,Nan, C. W. (2019). "Opportunities and challenges for magnetoelectric devices", *APL Materials*, Vol. 7, no. 8. doi:10.1063/1.5112089

[17] Landauer, R. (1961). "R. Landauer r Irreversibility and Heat Generation in the Computing P rocess", *IBM Journal of Research and Development*, Vol. 5, no. 3, pp. 183–191. doi:10.1147/rd.53.0183

[18] Manipatruni, S.,Nikonov, D. E.,Young, I. A. (2018). "Beyond CMOS computing with spin and polarization", *Nature Physics*, Vol. 14, no. 4, pp. 338–343.

doi:10.1038/s41567-018-0101-4

[19] Taz, H.,Prasad, B.,Huang, Y. L.,Chen, Z.,Hsu, S. L.,Xu, R.,Thakare, V.,Sakthivel, T. S.,Liu, C.,Hettick, M.,Mukherjee, R.,Seal, S.,Martin, L. W.,Javey, A.,Duscher, G.,Ramesh, R.,Kalyanaraman, R. (2020). "Integration of amorphous ferromagnetic oxides with multiferroic materials for room temperature magnetoelectric spintronics", *Scientific Reports*, Vol. 10, no. 1, pp. 3583. doi:10.1038/s41598-020-58592-5

[20] Sofi, S. A.,Gupta, D. C. (2020). "Systematic study of ferromagnetic phase stability of Co-based Heusler materials with high figure of merit: Hunt for spintronics and thermoelectric applicability", *AIP Advances*, Vol. 10, no. 10. doi:10.1063/5.0027070

[21] Fiebig, M.,Lottermoser, T.,Meier, D.,Trassin, M. (2016). "The evolution of multiferroics", *Nature Reviews Materials*, Vol. 1, no. 8, pp. 1–14. doi:10.1038/natrevmats.2016.46

[22] Liang, X.,Matyushov, A.,Hayes, P.,Schell, V.,Dong, C.,Chen, H.,He, Y.,Will-Cole, A.,Quandt, E.,Martins, P.,McCord, J.,Medarde, M.,Lanceros-Mendez, S.,Van Dijken, S.,Sun, N. X.,Sort, J. (2021). "Roadmap on Magnetoelectric Materials and Devices", *IEEE Transactions on Magnetics*, Vol. 57, no. 8, pp. 1–56. doi:10.1109/TMAG.2021.3086635

[23] Cao, G.,Cao, Y.,Huang, H.,Chen, L. Q.,Ma, X. (2016). "Analysis of multi-domain ferroelectric switching in BiFeO3 thin film using phase-field method", *Computational Materials Science*, Vol. 115, pp. 208–213. doi:10.1016/j.commatsci.2015.11.021

[24] Choy, T.-S.,Chen, J.,Hershfield, S. (1999). "Correlation between Spin Polarization and Magnetic Moment in Ferromagnetic Alloys", *Journal of Applied Physics*, Vol. 86, no. 1, pp. 562–564. doi:10.1063/1.370766

[25] Tariq, M.,Chaudhary, K.,Shaari, A.,Jalil, A.,Ismail, F. D.,Ahmed, R.,Haider, Z.,Hussain, R. (2022). "Ultralow energy switching with spin polarized magneto-electric properties of co-doped cubic phase BFO: A first-principles study", *Chinese Journal of Physics*, Vol. 79, pp. 211–224. doi:10.1016/j.cjph.2022.08.021

[26] Wang, W.,Sun, W.,Zhang, G.,Ren, F.,Wang, Y.,You, C.,Cheng, Z. (2020). "Ferroelectrically tunable magnetism in BiFeO3/BaTiO3 heterostructure revealed by the first-principles calculations", *Journal of Advanced Research*, Vol. 24, pp. 371–377. doi:10.1016/j.jare.2020.04.012

[27] Ukpong, A. M. (2021). "Emergence of nontrivial spin textures in frustrated van der waals ferromagnets", *Nanomaterials*, Vol. 11, no. 7, pp. 1770. doi:10.3390/nano11071770

[28] Kotnala, R. K.,Shah, J. (2015). "Ferrite Materials: Nano toSpintronics Regime", *Handbook of Magnetic Materials*, Vol. 23, pp. 291–379. doi:10.1016/B978-0-444-63528-0.00004-8

[29] Eerenstein, W.,Mathur, N. D.,Scott, J. F. (2006). "Multiferroic and magnetoelectric materials", *Nature*, Vol. 442, no. 7104, pp. 759–765. doi:10.1038/nature05023

[30] Vopson, M. M. (2015). "Fundamentals of Multiferroic Materials and Their Possible Applications", *Ritical Reviews in Solid State and Materials Sciences*, Vol. 40, no. 4, pp. 223–250. doi:10.1080/10408436.2014.992584

[31] Kharrazi, S.,Kundaliya, D. C.,Gosavi, S. W.,Kulkarni, S. K.,Venkatesan, T.,Ogale, S. B.,Urban, J.,Park, S.,Cheong, S. W. (2006). "Multiferroic TbMnO3 nanoparticles", *Solid State Communications*, Vol. 138, no. 8, pp. 395–398. doi:10.1016/j.ssc.2006.03.034

[32] Scott, J. F. (2013). "Room-temperature multiferroic magnetoelectrics", *NPG Asia Materials*, Vol. 5, no. 10, pp. e72–e72. doi:10.1038/am.2013.58

[33] Wang, Y.,Hu, J.,Lin, Y.,Nan, C. W. (2010). "Multiferroic magnetoelectric composite nanostructures", *NPG Asia Materials*, Vol. 2, no. 2, pp. 61–68. doi:10.1038/asiamat.2010.32

[34] Prellier, W.,Singh, M. P.,Murugavel, P. (2005). "The single-phase multiferroic oxides: From bulk to thin film", *Journal of Physics Condensed Matter*, Vol. 17, no. 30, pp. R803. doi:10.1088/0953-8984/17/30/R01

[35] Buurma, A. J. C.,Blake, G. R.,Palstra, T. T. M.,Adem, U. (2016). "Multiferroic Materials: Physics and Properties", *Reference Module in Materials Science and*

Materials Engineering. doi:10.1016/b978-0-12-803581-8.09245-6

[36] Tariq, M. (n.d.). "Frist Principle Investigation of Metals Doped Bismuth Ferrite for Switching Energy of Magneto-Electric Spin Orbit Capacitor"

[37] Spaldin, N. A.,Ramesh, R. (2019). "Advances in magnetoelectric multiferroics", *Nature Materials*, Vol. 18, no. 3, pp. 203–212. doi:10.1038/s41563-018-0275-2

[38] Goto, T.,Kimura, T.,Lawes, G.,Ramirez, A. P.,Tokura, Y. (2004). "Ferroelectricity and giant magnetocapacitance in perovskite rare-earth manganites", *Physical Review Letters*, Vol. 92, no. 25 I, pp. 257201. doi:10.1103/PhysRevLett.92.257201

[39] Kimura, T.,Lawes, G.,Goto, T.,Tokura, Y.,Ramirez, A. P. (2005). "Magnetoelectric phase diagrams of orthorhombic RMnO3 (R=Gd, Tb, and Dy)", *Physical Review B - Condensed Matter and Materials Physics*, Vol. 71, no. 22, pp. 224425. doi:10.1103/PhysRevB.71.224425

[40] Kenzelmann, M.,Harris, A. B.,Jonas, S.,Broholm, C.,Schefer, J.,Kim, S. B.,Zhang, C. L.,Cheong, S.-W.,Vajk, O. P.,Lynn, J. W. (2005). "Magnetic inversion symmetry breaking and ferroelectricity in TbMnO3", *Physical Review Letters*, Vol. 95, no. 8, pp. 087206. doi:10.1103/PhysRevLett.95.087206

[41] Kimura, T.,Goto, T.,Shintani, H.,Ishizaka, K.,Arima, T.,Tokura, Y. (2003). "Magnetic control of ferroelectric polarization", *Nature*, Vol. 426, no. 6962, pp. 55–58. doi:10.1038/nature02018

[42] Lawes, G.,Harris, A. B.,Kimura, T.,Rogado, N.,Cava, R. J.,Aharony, A.,Entin-Wohlman, O.,Yildirim, T.,Kenzelmann, M.,Broholm, C.,P Ramirez, and A.,Sackler, B. (2005). "Magnetically driven ferroelectric order in Ni3V2O8", *Physical Review Letters*, Vol. 95, no. 8, pp. 087205. doi:10.1103/PhysRevLett.95.087205

[43] Katsura, H.,Nagaosa, N.,Balatsky, A. V. (2004). "Spin current and magneto-electric effect in non-collinear magnets", *Physical Review Letters*, Vol. 95, no. 5, pp. 057205. doi:10.1103/PhysRevLett.95.057205

[44] Lu-Gang, C.,Fa-Min, L.,Wen-Wu, Z. (2010). "Structural, electronic and optical properties of orthorhombic distorted perovskite TbMnO3", *Chinese Physics B*,

Vol. 19, no. 9, pp. 97101. doi:10.1088/1674-1056/19/9/097101

[45] Collazos, J. C.,Bonilla, F. J.,Heiras, J.,Moran, O.,Bolaños, G. (2012). "Magnetic properties of al-doped TbMnO3 bulk samples", *Journal of Superconductivity and Novel Magnetism*, Vol. 25, no. 7, pp. 2231–2234. doi:10.1007/s10948-012-1664-4

[46] Izquierdo, J. L.,Astudillo, A.,Martínez, J.,Bolaños, G.,Morán, O. (2020). "Observation of drastic changes in the magnetic response of epitaxial TbMnO3 thin films upon Al-doping", *Journal of Physics and Chemistry of Solids*, Vol. 139, pp. 109302. doi:10.1016/j.jpcs.2019.109302

[47] Wang, S. L.,Li, P. G.,Zou, Y. H.,Wu, X. P.,Ungar, G.,Liu, Y. S.,Shen, J. Q.,Tang, W. H. (2015). "Crystal structure and electrical transport properties of polycrystalline TbMn1-xFexO3", *Journal of Physics and Chemistry of Solids*, Vol. 85, pp. 81–85. doi:10.1016/j.jpcs.2015.05.002

[48] Xu, J.,Cui, Y. (2013). "Dielectric characteristics of Ga doped TbMnO3", *Materials Science and Engineering: B*, Vol. 178, no. 5, pp. 316–320. doi:10.1016/j.mseb.2012.11.025

[49] Lu, C.,Cui, Y. (2014). "Dielectric characteristics of Si-added and Si-doped TbMnO3", *Physica B: Condensed Matter*, Vol. 432, pp. 58–63. doi:10.1016/j.physb.2013.09.030

[50] Pavan Kumar, N.,Venugopal Reddy, P. (2014). "Investigation of magnetocaloric effect in Dy doped TbMnO3", *Materials Letters*, Vol. 132, pp. 82–85. doi:10.1016/j.matlet.2014.06.012

[51] Pavan Kumar, N.,Jitender, T.,Laxmi, V.,Venugopal Reddy, P. (2016). "Thermal, magnetic and electrical properties of Tb1-xDyxMnO3 multiferroics", *Journal of Magnetism and Magnetic Materials*, Vol. 401, pp. 860–869. doi:10.1016/j.jmmm.2015.10.120

[52] Car, R. (2002). "Introduction to density-functional theory and ab-initio molecular dynamics", *Quantitative Structure-Activity Relationships*, Vol. 21, no. 2, pp. 97–104. doi:10.1002/1521-3838(200207)21:2<97::AID-QSAR97>3.0.CO;2-6

[53] TARIQ, M. (2023). "Computational simulation of Bismuth ferrite doped with transition metals for ultra-low switching energy of spintronic random-access memory"

[54] Guillén, O.,Jorge Mario. (2004). "Density functional theory in computational materials science"

[55] Xu, B.,Nan, C. W. (2018). "Modeling and predicting responses of magnetoelectric materials", *MRS Bulletin*, Vol. 43, no. 11, pp. 829–833. doi:10.1557/mrs.2018.259

[56] Zhu, L.,Zhou, J.,Guo, Z.,Sun, Z. (2015). "An overview of materials issues in resistive random access memory", *Journal of Materiomics*, Vol. 1, no. 4, pp. 285–295. doi:10.1016/j.jmat.2015.07.009

[57] Zhao, X. B. (2014). "Research on computer simulation in titanium dioxide photocatalytic experiment", *Advanced Materials Research*, Vols 1049–1050, pp. 64–68. doi:10.4028/www.scientific.net/AMR.1049-1050.64

[58] Hernández-Haro, N.,Ortega-Castro, J.,Martynov, Y. B.,Nazmitdinov, R. G.,Frontera, A. (2019). "DFT prediction of band gap in organic-inorganic metal halide perovskites: An exchange-correlation functional benchmark study", *Chemical Physics*, Vol. 516, pp. 225–231. doi:10.1016/j.chemphys.2018.09.023

[59] Clark, S. J.,Segall, M. D.,Pickard Ii, C. J.,Hasnip, P. J.,Probert, M. I. J.,Refson, K.,Payne, M. C. (2005). "First principles methods using CASTEP", *Zeitschrift Für Kristallographie-Crystalline Materials*, Vol. 220, nos. 5–6, pp. 567–570. doi:10.1524/zkri.220.5.567.65075

[60] Hossain, M. T. (2019). "First principles and experimental study on MoS2-based nanocomposites for fuel cell application"

[61] Sharma, V.,McDannald, A.,Staruch, M.,Ramprasad, R.,Jain, M. (2015). "Dopant-mediated structural and magnetic properties of TbMnO3", *Applied Physics Letters*, Vol. 107, no. 1. doi:10.1063/1.4926369

[62] Cai, L. G.,Liu, F. M.,Zhang, D.,Zhong, W. W. (2012). "Electronic and optical properties of distorted rare-earth manganite under hydrostatic pressure", *Solid State Communications*, Vol. 152, no. 12, pp. 1036–1041.

doi:10.1016/j.ssc.2012.03.024

[63] Abdelkader, H. S.,Berrahil, B.,Merad, G. (2019). "Effect of Ca doping on structural, magnetic and electronic properties of TbMnO3", *Journal of Magnetism and Magnetic Materials*, Vol. 477, pp. 77–82. doi:10.1016/j.jmmm.2019.01.022

[64] Cai, L. G.,Liu, F. M.,Zhong, W. W.,Zhang, D. (2013). "The electronic structures and optical properties of substituted rare-earth manganite Tb1-xYbxMnO3", *Chinese Physics Letters*, Vol. 30, no. 5, pp. 053601. doi:10.1088/0256-307X/30/5/053601

[65] Cuartero, V.,Blasco, J.,Rodríguez-Velamazán, J. A.,García, J.,Subías, G.,Ritter, C.,Stankiewicz, J.,Canadillas-Delgado, L. (2012). "Effects of Al substitution on the multiferroic properties of TbMnO3", *Physical Review B - Condensed Matter and Materials Physics*, Vol. 86, no. 10, pp. 104413. doi:10.1103/PhysRevB.86.104413

[66] Hemme, P.,Djemia, P.,Rovillain, P.,Gallais, Y.,Sacuto, A.,Forget, A.,Colson, D.,Charron, E.,Perrin, B.,Belliard, L.,Cazayous, M. (2021). "Elastic and magnetoelastic properties of TbMnO3 single crystal by nanosecond time resolved acoustics and first-principles calculations", *Journal of Physics: Condensed Matter*, Vol. 33, no. 49, pp. 495402. doi:10.1088/1361-648X/ac25ad

[67] Tse, G.,Yu, D. (2015). "The first principle study: electronic and optical properties in BiGaO3", *Asian Journal of Current Engineering and Maths*, Vol. 4, no. 5, pp. 56–61. doi:10.15520/ajcem.2015.vol4.iss5.38.pp56-61

[68] Lin, Z.,Lei, J.,Wang, P.,Zhang, X.,Xu, L.,Chen, M.,Kang, Y.,Wei, G. (2022). "Density functional study of structural, electronic and optical properties of bromine-doped CsPbI3 with the tetragonal symmetry", *Journal of Alloys and Compounds*, Vol. 892, pp. 162165. doi:10.1016/j.jallcom.2021.162165

[69] Cai, L. G.,Liu, F. M.,Zhong, W. W. (2010). "Structural, electronic and optical properties of orthorhombic distorted perovskite TbMnO3", *Chinese Physics B*, Vol. 19, no. 9, pp. 1–5. doi:10.1088/1674-1056/19/9/097101

[70] Prokhnenko, O.,Aliouane, N.,Feyerherm, R.,Dudzik, E.,Wolter, A. U.

B.,Maljuk, A.,Kiefer, K.,Argyriou, D. N. (2010). "Ga substitution as an effective variation of Mn-Tb coupling in multiferroic TbMnO3", *Physical Review B*, Vol. 81, no. 2, pp. 024419. doi:10.1103/PhysRevB.81.024419

[71] Blasco, J.,Ritter, C.,Garcí, J.,De Teresa, J. M.,Pé Rez-Cacho, J.,Ibarra, M. R. (2000). "Structural and magnetic study of Tb 1Àx Ca x MnO 3 perovskites", *Physical Review B*, Vol. 62, no. 9, pp. 5609. doi:10.1103/PhysRevB.62.5609

[72] Cui, Y.,Wang, C.,Cao, B. (2005). "TbMnO3 epitaxial thin films by pulsed-laser deposition", *Solid State Communications*, Vol. 133, no. 10, pp. 641–645. doi:10.1016/j.ssc.2005.01.002

[73] Mulliken, R. S. (1955). "Electronic population analysis on LCAO-MO molecular wave functions. I", *The Journal of Chemical Physics*, Vol. 23, no. 10, pp. 1833–1840. doi:10.1063/1.1740588

[74] Chakraborty, A.,Liton, M. N. H.,Sarker, M. S. I.,Rahman, M. M.,Khan, M. K. R. (2023). "A comprehensive DFT evaluation of catalytic and optoelectronic properties of BaTiO3 polymorphs", *Physica B: Condensed Matter*, Vol. 648, pp. 414418. doi:10.1016/j.physb.2022.414418

[75] Harcourt, R. D. (1974). "Diatomic antibonding σ*s orbitals as ‘metallic orbitals’ for electron conduction in alkali metals", *Ournal of Physics B: Atomic and Molecular Physics*, Vol. 7, no. 2, pp. L41. doi:10.1088/0022-3700/7/2/003

[76] Dresselhaus, M. S. (2001). "Solid state physics part II optical properties of solids", *Lecture Notes Part 2*

[77] Kittel, C. (2005). "Introduction to solid state physics"

[78] Zhang, Y.,Tong, T.,Kinsman, W.,Jiang, P.,Yin, G.,Li, S. (2013). "Dielectric and impedance analysis of la doped-TbMnO3", *Journal of Alloys and Compounds*, Vol. 549, pp. 358–361. doi:10.1016/j.jallcom.2012.09.005

[79] Halder, M.,Meikap, A. K. (2020). "Dielectric relaxation and magnetodielectric response of mesoporous terbium manganate nanopaticles", *SN Applied Sciences*, Vol. 2, no. 4, pp. 1–11. doi:10.1007/s42452-020-2562-1